The Astronomical Journal, 167:162 (14pp), 2024 April https://doi.org/10.3847/1538-3881/ad284f

OGLE-2017-BLG-0448Lb: A Low Mass–Ratio Wide-orbit Microlensing Planet?

Ruocheng Zhai[1], Radosław Poleski[2], Weicheng Zang[1,3], Youn Kil Jung[4,5], Andrzej Udalski[2], Renkun Kuang[1,6], (Leading Authors),
Michael D. Albrow[7], Sun-Ju Chung[4], Andrew Gould[8,9], Cheongho Han[10], Kyu-Ha Hwang[4], Yoon-Hyun Ryu[4], In-Gu Shin[3], Yossi Shvartzvald[11], Hongjing Yang[1], Jennifer C. Yee[3], Sang-Mok Cha[4,12], Dong-Jin Kim[4], Hyoun-Woo Kim[4], Seung-Lee Kim[4], Chung-Uk Lee[4], Dong-Joo Lee[4], Yongseok Lee[4,12], Byeong-Gon Park[4,5], Richard W. Pogge[9], (The KMTNet Collaboration),
Jan Skowron[2], Michał K. Szymański[2], Igor Soszyński[2], Krzysztof Ulaczyk[13], Paweł Pietrukowicz[2], Szymon Kozłowski[2], Przemek Mróz[2], Krzysztof A. Rybicki[2,11], Patryk Iwanek[2], Marcin Wrona[2], Mariusz Gromadzki[2], (The OGLE Collaboration), and
Hanyue Wang[3], Shude Mao[1], Jiyuan Zhang[1], Qiyue Qian[1], and Wei Zhu[1] (The MAP Collaboration)

[1] Department of Astronomy, Tsinghua University, Beijing 100084, People's Republic of China
[2] Astronomical Observatory, University of Warsaw, Al. Ujazdowskie 4, 00-478 Warszawa, Poland
[3] Center for Astrophysics | Harvard & Smithsonian, 60 Garden Street, Cambridge, MA 02138, USA
[4] Korea Astronomy and Space Science Institute, Daejon 34055, Republic of Korea
[5] University of Science and Technology, Korea, (UST), 217 Gajeong-ro Yuseong-gu, Daejeon 34113, Republic of Korea
[6] Department of Engineering Physics, Tsinghua University, Beijing 100084, People's Republic of China
[7] University of Canterbury, Department of Physics and Astronomy, Private Bag 4800, Christchurch 8020, New Zealand
[8] Max-Planck-Institute for Astronomy, Königstuhl 17, 69117 Heidelberg, Germany
[9] Department of Astronomy, Ohio State University, 140 W. 18th Avenue, Columbus, OH 43210, USA
[10] Department of Physics, Chungbuk National University, Cheongju 28644, Republic of Korea
[11] Department of Particle Physics and Astrophysics, Weizmann Institute of Science, Rehovot 76100, Israel
[12] School of Space Research, Kyung Hee University, Yongin, Kyeonggi 17104, Republic of Korea
[13] Department of Physics, University of Warwick, Gibbet Hill Road, Coventry, CV4 7AL, UK
Received 2023 December 13; revised 2024 February 6; accepted 2024 February 10; published 2024 March 18

Abstract

The gravitational microlensing technique is most sensitive to planets in a Jupiter-like orbit and has detected more than 200 planets. However, only a few wide-orbit ($s > 2$) microlensing planets have been discovered, where s is the planet-to-host separation normalized to the angular Einstein ring radius, $\theta_{\rm E}$. Here, we present the discovery and analysis of a strong candidate wide-orbit microlensing planet in the event OGLE-2017-BLG-0448. The whole light curve exhibits long-term residuals to the static binary-lens single-source model, so we investigate the residuals by adding the microlensing parallax, microlensing xallarap, an additional lens, or an additional source. For the first time, we observe a complex degeneracy between all four effects. The wide-orbit models with $s \sim 2.5$ and a planet-to-host mass ratio of $q \sim 10^{-4}$ are significantly preferred, but we cannot rule out the close models with $s \sim 0.35$ and $q \sim 10^{-3}$. A Bayesian analysis based on a Galactic model indicates that, despite the complicated degeneracy, the surviving wide-orbit models all contain a super-Earth-mass to Neptune-mass planet at a projected planet-host separation of ∼6 au and the surviving close-orbit models all consist of a Jovian-mass planet at ∼1 au. The host star is probably an M or K dwarf. We discuss the implications of this dimension-degeneracy disaster on microlensing light-curve analysis and its potential impact on statistical studies.

Unified Astronomy Thesaurus concepts: Gravitational microlensing exoplanet detection (2147)

1. Introduction

The solar system planets are typically divided into three groups: rocky planets, gas giants, and ice giants. The two groups of giant planets are more important than the rocky planets from the perspective of planetary system formation and evolution: the amount of water on Earth is influenced by the time when Jupiter's core formed (Morbidelli et al. 2016), the changes of orbits of most massive planets significantly changed orbits of other planets and dwarf planets (Thommes et al. 1999; Tsiganis et al. 2005; Batygin & Brown 2016) even leading to an ejection of a planet (Batygin et al. 2012; Nesvorný & Morbidelli 2012), to name just a few aspects.

In the solar system, all giant planets have orbits wider than the ice line (2.7 au; Kennedy & Kenyon 2008). Hence, in order to understand the solar system formation in a broader context, we should be interested in searching for exoplanets orbiting other stars on similarly wide orbits. Currently, there are only two exoplanet detection techniques that efficiently find planets on wide orbits: direct imaging and gravitational microlensing (Mao & Paczynski 1991; Gould & Loeb 1992). Microlensing has a unique capability to find wide-orbit exoplanets with mass

ratios of Jupiter to the Sun (10^{-3}) or lower (Gaudi 2012). The two planet parameters that are routinely measured are the mass ratio (q) and projected separation (s), which is measured relative to the angular Einstein ring radius ($\theta_{\rm E}$). In a typical case, the Einstein ring radius corresponds to the projected planet–star separations on the order of 2.5 au. Hence, to study exoplanets on orbits similar to the solar system giant planets, we should focus on microlensing exoplanets that have $s \gg 1$.

Here we present a detailed analysis of OGLE-2017-BLG-0448Lb, which is a strong candidate for a wide-orbit planet with a low mass ratio. This wide-orbit solution can be compared to the widest-orbit microlensing planet: OGLE-2008-BLG-092LAb with $s = 5.26 \pm 0.11$ and $q = (2.41 \pm 0.45) \times 10^{-4}$ (Poleski et al. 2014). Recent microlensing studies have focused on planets with mass ratios of 10^{-4} and smaller because of possible break of the mass-ratio distribution function (Suzuki et al. 2016; Udalski et al. 2018; Jung et al. 2019a). Among the $q < 10^{-4}$ planets, the widest secure separation is $s = 1.610 \pm 0.008$ for OGLE-2005-BLG-390Lb ($q = (0.76 \pm 0.07) \times 10^{-4}$; Beaulieu et al. 2006). A larger separation of $s = 1.773 \pm 0.006$ (and $q = (0.187 \pm 0.015) \times 10^{-4}$) is possible for OGLE-2018-BLG-0596Lb, but the light curve of this planet favors the close solution ($s = 0.564 \pm 0.005$ and $q = (1.33 \pm 0.11) \times 10^{-4}$) by $\Delta\chi^2 = 17$ (Jung et al. 2019b). The wide solution for OGLE-2017-BLG-0448Lb has q smaller by a factor of 6.7 than OGLE-2008-BLG-092LAb and a separation wider by a factor of $\gtrsim$1.5 than OGLE-2005-BLG-390Lb or OGLE-2018-BLG-0596Lb. Hence, OGLE-2017-BLG-0448Lb is unique in probing the mass-ratio distribution at the wide separations.

The detection of the planetary anomaly in this event was first mentioned by Zang et al. (2023) who presented a systematic search (Zang et al. 2021a, 2022) for planets in the Korean Microlensing Telescope Network (KMTNet; Kim et al. 2016) photometric database from 2016–2019. However, the complexity of the event analysis required a detailed investigation presented here.

2. Observations

The source of the microlensing event OGLE-2017-BLG-0448 lies toward the Galactic bulge at the equatorial coordinates $(\alpha, \delta)_{\rm J2000} = (17{:}54{:}40.47, -31{:}01{:}54.9)$, corresponding to Galactic coordinates $(\ell, b) = (-0.7948, -2.7576)$. The event was found first by the Optical Gravitational Lensing Experiment (OGLE) and announced on 31 March 2017 by the OGLE Early Warning System (Udalski 2003; Udalski et al. 2015). The event was then independently discovered by the KMTNet post-season EventFinder system (Kim et al. 2018) based on all the data collected during the 2017 season.

The OGLE survey obtains photometry using a 1.3 m telescope with a 1.4 deg^2 camera at the Las Campanas Observatory (Chile; Udalski et al. 2015). The event was located in the OGLE field BLG534, which is observed with a cadence of 1 hr^{-1}. The KMTNet survey conducted observations from three identical 1.6 m telescopes equipped with 4 deg^2 cameras in Chile (KMTC), South Africa (KMTS), and Australia (KMTA). The event lies in two slightly offset KMT fields, BLG01 and BLG41, with a combined cadence of 4 hr^{-1} for KMTC and 3 hr^{-1} for KMTA and KMTS. For both surveys, most of the images were taken in the I band, and a small fraction of V-band images were acquired for source color measurements. For this event, the V-band data of KMTC41 and KMTS01 cover the planetary signal, so we include them in the light-curve analysis. The V-band photometry helps to exclude the single-lens binary-source (1L2S) models.

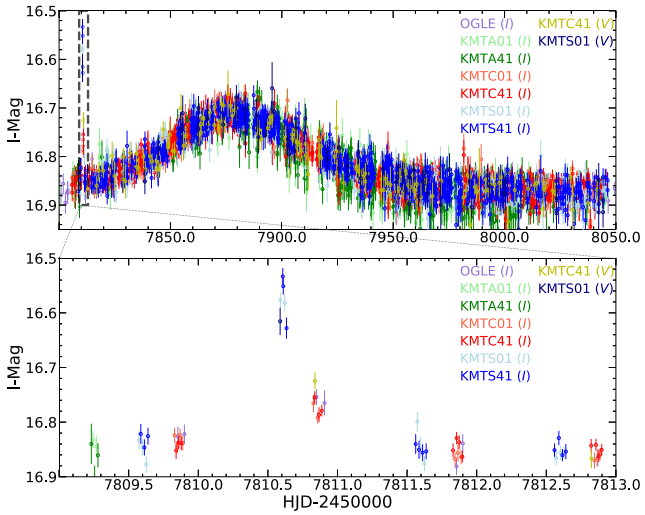

Figure 1. Observed light curve of the microlensing event, OGLE-2017-BLG-0448. Different colors represent the observed data from different data sets. The upper panel shows all of the data taken in 2017, and the lower panel displays a close-up of the planetary signal.

The photometry was extracted from the OGLE and KMTNet images using the custom photometry pipelines that are based on the different imaging technique (Tomaney & Crotts 1996; Alard & Lupton 1998): pySIS (Albrow et al. 2009; Yang et al. 2024) for the KMTNet data, and Wozniak (2000) for the OGLE data. For the KMTC01 data, we additionally extracted photometry using the pyDIA software (Albrow 2017) in order to measure the source color and construct the color–magnitude diagram (CMD). The I-band magnitude of the light curve has been calibrated to the OGLE-III I-band magnitude (Szymański et al. 2011). The error bars for the OGLE and KMTNet data from the individual photometry pipelines were readjusted following the processes of Skowron et al. (2016) and Yee et al. (2012), respectively. We note that the smallest $\chi^2/d.o.f.$ found in our analysis is slightly lower than one (0.94; Section 3.3.2) because we use Skowron et al. (2016) error bar estimation for the OGLE data. Using the procedure from Yee et al. (2012) for the OGLE data does not influence our conclusions.

3. Binary-lens Single-source Model

We display the light curve of the microlensing event, OGLE-2017-BLG-0448, in Figure 1. The event started rising in early 2017. The first maximum of the brightness was observed at HJD$' = 7810$ (HJD$'$= HJD—2450000). This maximum is mostly covered by the KMTS data. Its full amplitude is not precisely measured but it must be at least 0.25 mag. This maximum lasted one day or less; hence, it was relatively short, and we call it an anomaly henceforth. The exact shape of the anomaly is not well constrained because of a lack of data between HJD$' = 7809.9$ and 7810.6. Following the anomaly, the event shows a long bell-shaped curve with an amplitude of 0.15 mag and a peak at HJD$' \approx 7882$. A microlensing light curve with two maxima of similar shape can be interpreted as either a 1L2S event or a binary-lens single-source (2L1S) event (Gaudi 1998). In the latter case, a large difference in the duration of the two maxima points to a low mass ratio, i.e., in the planetary regime (Gaudi & Gould 1997). Additionally, the

two peaks have a relatively long time separation, which points to a very wide ($s \gg 1$) or a very close ($s \ll 1$) lens topology (Han 2006). We present the 2L1S analysis below and show the 1L2S analysis in Section 5.

3.1. Static Binary-lens Model

The 2L1S model with a finite source is parametrized by seven variables. The first four are the same as for the single-lens single-source (1L1S; Paczyński 1986) model: t_0—the epoch of minimum lens–source separation, u_0—the source–lens impact parameter relative to θ_E, t_E—the Einstein ring crossing time, and ρ—the ratio of the angular source size to θ_E. The other three parameters are s, q, and α—the angle between lens–source trajectory and the axis of the binary lens. In the case of OGLE-2017-BLG-0448, the epoch of the anomaly is well constrained by the data, and its duration is constrained to be short, but these two properties do not easily map on the (s, q, α) parameters. Hence, we decided to re-parameterize the model in order to improve the convergence and acceptance ratios of the Markov chain Monte Carlo (MCMC) chains.[14] Instead of (s, q, α) we use: $t_{0,pl}$—the epoch of approach to the planetary caustic, $u_{0,pl}$—the source–planetary caustic impact parameter relative to θ_E, and $t_{E,\,pl}$—the planetary Einstein ring crossing time. We derive the equations to transform between the two sets of parameters based on a simple geometric consideration and the distance between planetary and central caustic ($s' = |s - 1/s|$; Han 2006). For the wide topology, these equations are:

$$q = \left(\frac{t_{E,pl}}{t_E}\right)^2, \tag{1}$$

$$\tau_{pl} = \frac{t_0 - t_{0,pl}}{t_E}, \tag{2}$$

$$s' = \sqrt{(u_0 + u_{0,pl})^2 + \tau_{pl}^2}, \tag{3}$$

$$s = \frac{\sqrt{s'^2 + 4} + s'}{2}, \tag{4}$$

$$\alpha = \arcsin\frac{u_0 + u_{0,pl}}{s'}. \tag{5}$$

For the close topology, the last two of these equations are modified:

$$s = \frac{\sqrt{s'^2 + 4} - s'}{2}, \tag{6}$$

$$\alpha = \arcsin\frac{u_0 + u_{0,pl}}{s'} + 180°. \tag{7}$$

The above equations are also used for the binary-lens models with additional higher-order effects: parallax and xallarap. We note that the physical interpretation of $t_{0,pl}$, $u_{0,pl}$, and $t_{E,\,pl}$ provided above is only approximate for models with these higher-order effects.

We employ the advanced contour-integration code (Bozza 2010; Bozza et al. 2018) to calculate the 2L1S magnification. In addition, we introduce two linear parameters ($f_{S,i}, f_{B,i}$) for each data set i to represent the source flux and any blended flux. Both OGLE and KMTNet detected the event from the change in flux of a catalog star for which the OGLE-III catalog (Szymański et al. 2011) gives the brightness of $I = 16.978 \pm 0.017$. Both surveys also reported a >200 mas offset between the magnified source and the catalog star. We thus check the i'-band baseline images taken by the 3.6 m Canada–France–Hawaii Telescope (CFHT), with seeing FWHM of 0.″45–0.″50. We calibrate the CFHT i'-band magnitude to the OGLE-III I-band magnitude using the field stars within 2′ around the event. The CFHT images resolve two stars, with a brightness of $I = 17.29 \pm 0.02$ and $I = 18.11 \pm 0.07$, respectively, and the microlensing event occurred on the $I = 17.29 \pm 0.02$ star. Thus, we add the following prior to the blend flux f_B:

$$\mathcal{L}_{prior} = \begin{cases} 1 & \text{if } f_B \geqslant 0, \\ \exp\left(-\dfrac{f_B^2}{2\sigma^2}\right) & \text{if } f_B < 0, \end{cases} \tag{8}$$

where σ is the flux uncertainty of the $I = 17.29 \pm 0.02$ star. The posterior results are presented in Table 1 with the MCMC fitting parameters presented first and additionally the (s, q, α) distributions provided at the end. We find four solutions, including two with minor-image (triangular, $s < 1$) planetary caustics and two with major-image (quadrilateral, $s > 1$) planetary caustics, as shown in Figure 2. For every pair of solutions, the intersection between the source trajectory and the binary axis is either inside or outside the planetary caustics relative to the central caustic. Thus, we label the two $s < 1$ solutions as "Close Inner" and "Close Outer" and the two $s > 1$ solutions as "Wide Inner" and "Wide Outer." Figure 3 displays the light curves of the four solutions, and all of the four solutions can reasonably fit the data around the anomaly (i.e., the first maximum). However, as shown in the top two panels of Figure 3, the static 2L1S model leaves long-term residuals before HJD′ = 7900. Therefore, we further include high-order effects.

3.2. 2L1S Parallax Model

We first try to improve the fit and remove the long-term residuals with the annual microlens-parallax effect (Gould 1992, 2000), in which Earth's acceleration around the Sun introduces nonlinear motion to the lens–source relative motion. We introduce two parameters $\pi_{E,\,N}$ and $\pi_{E,\,E}$, the north and east components of the microlensing parallax vector $\boldsymbol{\pi}_E$ in equatorial coordinates,

$$\boldsymbol{\pi}_E \equiv \frac{\pi_{rel}}{\theta_E}\frac{\boldsymbol{\mu}_{rel}}{\mu_{rel}}, \tag{9}$$

where π_{rel} and $\boldsymbol{\mu}_{rel}$ are the lens–source relative parallax and proper motion, respectively. We also fit the $u_0 > 0$ and $u_0 < 0$ solutions to account for the "ecliptic degeneracy" (Jiang et al. 2004; Poindexter et al. 2005). The annual microlens-parallax effect can be degenerated with the lens orbital motion effect (Batista et al. 2011; Skowron et al. 2011). Hence, we also introduce this effect. The lens orbital motion is parametrized by $\gamma = \left(\frac{ds/dt}{s}, \frac{d\alpha}{dt}\right)$, where ds/dt and $d\alpha/dt$ represent the instantaneous changes in the separation and orientation of the two lens components defined at HJD′ = 7880. We restrict the

[14] We apply the `emcee` ensemble sampler (Foreman-Mackey et al. 2013) for the MCMC χ^2 minimization.

Table 1
Lensing Parameters for 2L1S Static Models

Parameters	Close Inner	Close Outer	Wide Inner	Wide Outer
χ^2 /dof	**10237.7/10687**	10331.2/10687	10281.1/10687	10277.8/10687
t_0	$\mathbf{7879.92^{+0.08}_{-0.08}}$	$7879.99^{+0.09}_{-0.09}$	$7879.95^{+0.09}_{-0.09}$	$7879.94^{+0.09}_{-0.09}$
u_0	$\mathbf{1.225^{+0.017}_{-0.031}}$	$1.225^{+0.014}_{-0.031}$	$1.221^{+0.017}_{-0.034}$	$1.224^{+0.016}_{-0.030}$
$t_{\rm E}$(days)	$\mathbf{32.51^{+0.59}_{-0.39}}$	$32.39^{+0.59}_{-0.32}$	$32.49^{+0.65}_{-0.36}$	$32.45^{+0.56}_{-0.34}$
ρ (10^{-2})	$\mathbf{0.078^{+0.041}_{-0.035}}$	$0.294^{+0.028}_{-0.051}$	$1.041^{+0.074}_{-0.168}$	$0.665^{+0.244}_{-0.378}$
$t_{0,\rm pl}$	$\mathbf{7813.08^{+0.11}_{-0.13}}$	$7808.43^{+0.12}_{-0.13}$	$7810.45^{+0.04}_{-0.03}$	$7810.63^{+0.02}_{-0.02}$
$u_{0,\rm pl}$	$\mathbf{0.123^{+0.006}_{-0.006}}$	$-0.128^{+0.008}_{-0.008}$	$0.005^{+0.002}_{-0.003}$	$-0.007^{+0.002}_{-0.001}$
$t_{\rm E,\ pl}$ (days)	$\mathbf{0.88^{+0.04}_{-0.04}}$	$0.90^{+0.06}_{-0.05}$	$0.18^{+0.02}_{-0.02}$	$0.20^{+0.01}_{-0.02}$
$I_{\rm S}$	$\mathbf{17.30^{+0.06}_{-0.04}}$	$17.30^{+0.06}_{-0.03}$	$17.31^{+0.07}_{-0.04}$	$17.30^{+0.06}_{-0.03}$
s	$\mathbf{0.3554^{+0.0054}_{-0.0033}}$	$0.3545^{+0.0055}_{-0.0028}$	$2.8198^{+0.0256}_{-0.0474}$	$2.8141^{+0.0238}_{-0.0407}$
q (10^{-4})	$\mathbf{7.384^{+0.685}_{-0.672}}$	$7.623^{+0.980}_{-0.881}$	$0.309^{+0.088}_{-0.064}$	$0.362^{+0.055}_{-0.067}$
α (deg)	$\mathbf{33.2^{+0.2}_{-0.3}}$	$26.3^{+0.3}_{-0.3}$	$209.8^{+0.2}_{-0.2}$	$209.6^{+0.2}_{-0.2}$

Note. We present the fitted and derived parameters above and below the horizontal line, respectively. The best-fit 2L1S static model is boldfaced. The bold column indicates the preferred model.

MCMC trials to bound systems by calculating the ratio of projected kinetic to potential energy (An et al. 2002; Dong et al. 2009):

$$\beta \equiv \left| \frac{\mathrm{KE}_\perp}{\mathrm{PE}_\perp} \right| = \frac{\kappa M_\odot \mathrm{yr}^2}{8\pi^2} \frac{\pi_{\rm E}}{\theta_{\rm E}} \gamma^2 \left(\frac{s}{\pi_{\rm E} + \pi_{\rm S}/\theta_{\rm E}} \right)^3, \quad (10)$$

where $\pi_{\rm S}$ is the source parallax. We adopt $\pi_{\rm S} = 0.12$ mas based on the mean distance to clump giant stars in this direction (Nataf et al. 2013). We reject models with $\beta \geqslant 0.8$ for unphysical lens systems.

The resulting parameters are listed in Table 2. The inner and outer solutions of the Wide topology merge into one solution with the high-order effects, so there are three pairs of solutions. The "Wide $u_0 > 0$" solution provides the best fit to the observed data, for which the inclusion of the high-order effects significantly improves the fit by $\Delta\chi^2 = 192$ and removes the long-term residuals (Figure 4). However, this solution has a large parallax value of 1.40 ± 0.14. Such a large parallax (i.e., $\gtrsim$1) value is of very low probability though not impossible (e.g., Gould et al. 2009; Ryu et al. 2019). The "Close Outer $u_0 > 0$," "Close Inner $u_0 < 0$" and "Wide $u_0 < 0$" solutions also have a large parallax of $\gtrsim$1. The "Close Inner $u_0 > 0$" and "Close Outer $u_0 < 0$" solutions have reasonable parallax values of $0.38^{+0.09}_{-0.05}$ and $0.55^{+0.40}_{-0.18}$, respectively, but they are disfavored by $\Delta\chi^2 = 33.7$ and 15.8 compared to the "Wide $u_0 > 0$" solution, respectively. Therefore, we try the other high-order effect, the microlens–xallarap effect, to see whether a reasonable microlens–xallarap model can fit the long-term residuals.

3.3. 2L1S Xallarap Model

The long-term asymmetry in the light curve can be caused not only by the motion of the observer around the Sun (the microlens-parallax effect) but also by the inverse effect of motion of the source star in a binary system, called the xallarap effect (Griest & Hu 1992). Here, we consider the xallarap effect with a circular orbit. This effect introduces five additional parameters that can be defined in various ways (e.g., Miyazaki et al. 2020; Rota et al. 2021). Below we first introduce a new parameterization of the xallarap effect. Then, we discuss our approach to fitting and its results.

3.3.1. Parameterization of the Xallarap Effect

We define the xallarap orbit using five fitted parameters (ξ_P, ξ_a, ξ_i, ξ_Ω, ξ_u) and one fixed parameter ($t_{0,\xi}$). The fitted parameters are the usual Keplerian parameters of the orbit: ξ_P—the orbital period, ξ_a—the semimajor axis relative to $\theta_{\rm E}$, ξ_i—the inclincation, ξ_Ω—the longitude of the ascending node, and ξ_u —the argument of latitude at the reference epoch $t_{0,\xi}$.[15] We prefer to use the argument of latitude (instead of, e.g., the time of the periapsis passage) because periapsis is not defined for a circular orbit and is poorly constrained for an eccentric orbit with a small eccentricity. We define the orbital parameters with the reference plane to be the plane of the sky and the reference direction to be the relative lens–source proper motion direction.

To calculate the influence of the xallarap effect on the relative lens–source position, we calculate the position ($\boldsymbol{r}_1(t)$) of the luminous source relative to the center of mass on the reference plane for every epoch using standard orbit integration. We also calculate this position for the reference epoch: $\boldsymbol{r}_1(t_{0,\xi})$. The xallarap shift is calculated as $\boldsymbol{r}_1(t) - \boldsymbol{r}_1(t_{0,\xi})$. In this approach, the xallarap effect weakly affects the magnification for epochs close to $t_{0,\xi}$. The xallarap shift for the source center of mass is $-\boldsymbol{r}_1(t_{0,\xi})$. Furthermore, one can calculate the position of the second source component: the position of the second source relative to the center of mass is $-\boldsymbol{r}_1(t)/q_s$ (where q_s is the mass ratio of the source); hence, the xallarap shift for the second source is $-\boldsymbol{r}_1(t)/q_s - \boldsymbol{r}_1(t_{0,\xi})$.

We note that $t_{0,\xi}$ serves two purposes: it defines the reference epoch for ξ_u and it defines the epoch at which the xallarap does not affect the magnification. The specific choice of $t_{0,\xi}$ value does not have an impact on the former purpose. On the other hand, the specific choice of $t_{0,\xi}$ value for the latter purpose is a very important factor for the convergence of the MCMC chain

[15] The argument of latitude is the sum of the argument of periapsis and the true anomaly at a given epoch: $u(t) = \nu(t) + \omega$, and for a circular orbit, we have $u(t) \equiv \nu(t)$.

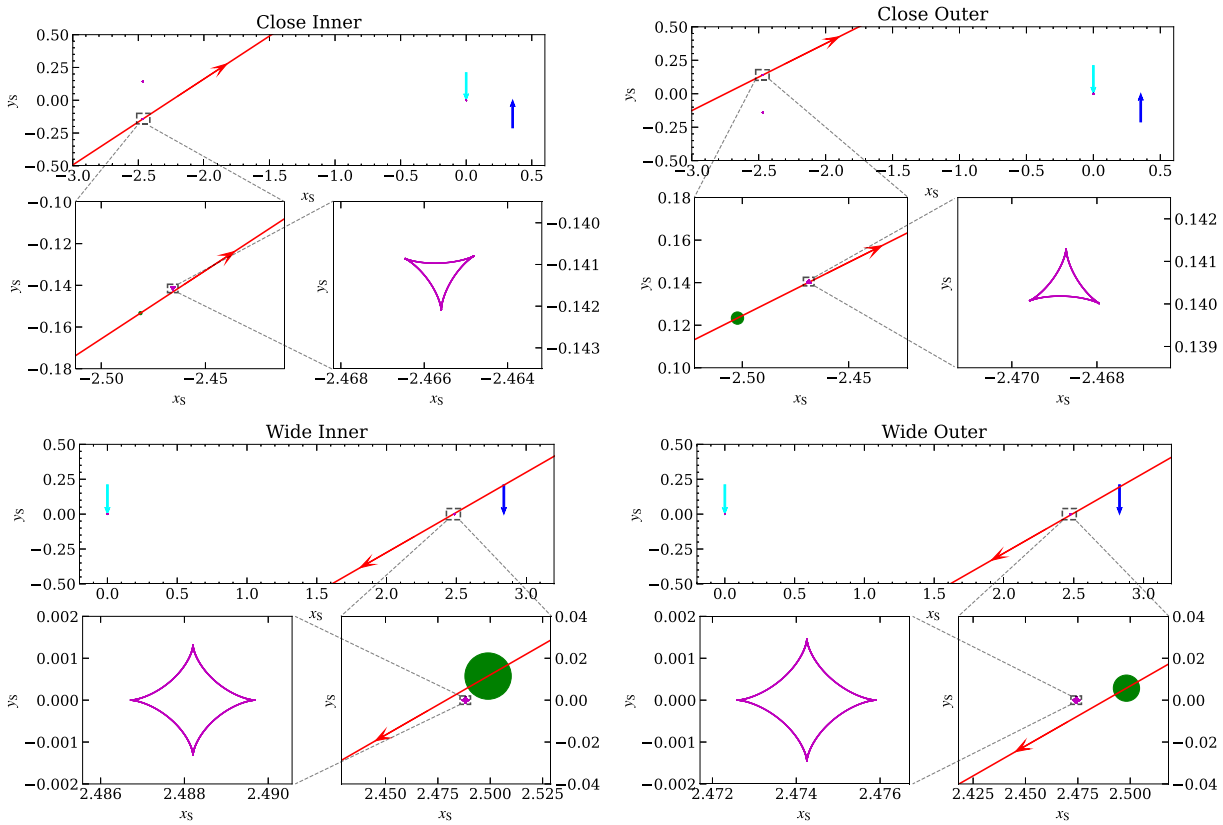

Figure 2. Caustic geometries of the four static 2L1S solutions. The locations of the host star and planet are indicated by cyan and blue arrows, respectively. The magenta lines show the caustic structures, and the red lines with an arrow indicate the source trajectory and the direction of the source motion. The radii of the green dots represent the best-fit normalized source radius, ρ, of each solution.

when one starts the parameter exploration from the best-fit model without xallarap.

3.3.2. Xallarap Model Fitting

We set $t_{0,\xi}$ close to the best-timed part of the event, i.e., anomaly: $t_{0,\xi} \equiv 7810.5$. The xallarap introduces five additional parameters, and in the case of OGLE-2017-BLG-0448, none of these parameters can be easily estimated from the light-curve inspection. We search the parameter space by starting from the static binary-lens models presented in Table 1. For each of these four models, we run an MCMC starting with the initial positions of the MCMC walkers drawn from uniform distributions (0, 360) of angles ξ_Ω, ξ_i, and ξ_u. The values of ξ_a were drawn log-uniformly from (0.001, 0.1). For the xallarap period ξ_P, we adopt a grid approach. We run the MCMC 10 times independently each one exploring a range of periods: $(3\xi_{P,i}/4,\ 4\xi_{P,i}/3)$, where $\xi_{P,i}$ is a geometric series of ten elements from 5 to 400 days. We can cover the range of periods from 3.7 to 540 days with overlapping runs, which ensures that the right period should be found even if it is very close to the edge of one of the period ranges. For each run, the initial positions of walkers are drawn from a normal distribution with the mean of $\xi_{P,i}$ and sigma of 0.001 days. From each of the ten runs, we extract the smallest χ^2 model. Then, we rerun the fitting with starting points randomly drawn very close to these smallest χ^2 models but without limiting the ξ_P values. We then identified and ignored duplicated results and runs that converged to models with much higher χ^2. Because the 2L1S parallax models find that the lens orbital motion effect has almost no influence on the models, the xallarap fitting does not include this effect.

This model exploration resulted in eight solutions within $\Delta\chi^2 < 30$, including three (labeled as "A," "B," and "C") for the "Wide" topology, three (labeled as "A," "B," and "C") for the "Close Outer" topology and two (labeled as "A" and "B") for the "Close Inner" topology. Their parameters are presented in Tables 3 and 4, and their source trajectories are shown in Figure 5. All of the eight 2L1S xallarap solutions provide better fits than the best-fit 2L1S parallax solution, with $\Delta\chi^2$ of between 1.1 and 14.3. Therefore, we keep all of the 2L1S xallarap solutions and evaluate all the 2L1S solutions with high-order effects by combining the physical parameters of the lens and the source systems.

4. Color–Magnitude Diagram

Before the 1L2S analysis, we analyze the CMD to obtain the source color and the source angular radius, θ_*, which are used to exclude the 1L2S model in Section 5.1 and estimate the lens physical parameters in Section 6. We locate the source on a $V-I$ versus I CMD, as shown in Figure 6. The CMD is constructed using the OGLE-III catalog stars (Szymański et al. 2011) within 120″ centered on the event. The centroid of the red giant clump is $(V-I,\ I)_{\rm cl} = (2.09 \pm 0.01,\ 15.73 \pm 0.01)$. From Bensby et al. (2013) and Nataf et al. (2013), the intrinsic color and de-reddened magnitude of the red giant clump are $(V-I,\ I)_{\rm cl,0} = (1.06 \pm 0.03,\ 14.49 \pm 0.04)$, indicating $A_I = 1.24 \pm 0.04$ and $E(V-I) = 1.03 \pm 0.03$ toward this direction.

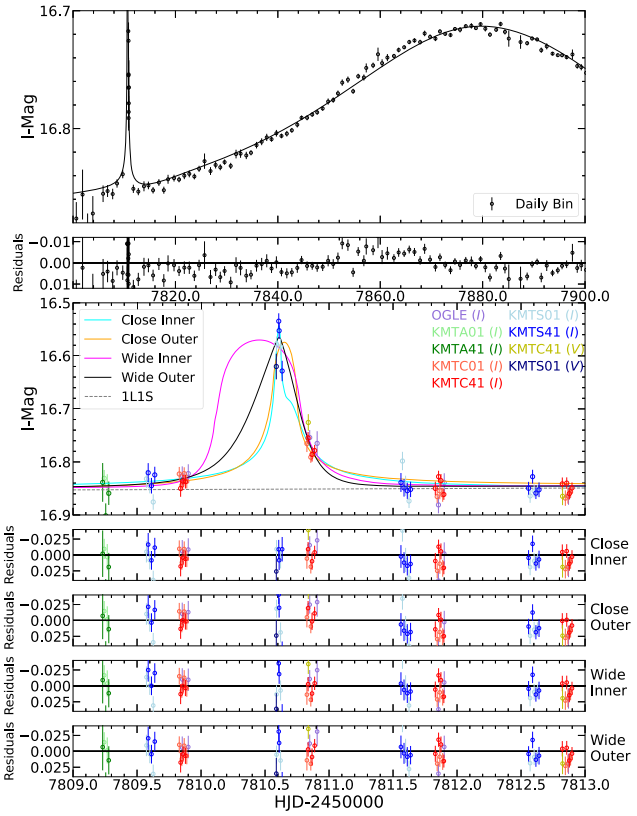

Figure 3. Observed data together with the four static 2L1S solutions. Data shown in the top two panels are daily binned. All four solutions can fit the anomaly well (the lower five panels), but there are long-term residuals before HJD′ = 7900, so we include high-order effects.

For the source color, we first measure $(V-I)_{\rm S,\ KMTC} = 2.01 \pm 0.04$ by regression of the KMTC01 V versus I flux and then obtain $(V-I)_{\rm S} = 1.95 \pm 0.04$ by matching the KMTC01 pyDIA CMD and the OGLE-III CMD. Then, the intrinsic source color is $(V-I)_{\rm S,0} = 0.92 \pm 0.05$. Because the source apparent brightness varies from the models, we first obtain the source angular radius θ_* for $I_{\rm S} = 17.35$ and then provide a scaling relation for different source brightnesses. Using the color/surface-brightness relation of Adams et al. (2018), we obtain

$$\theta_* = 2.33 \pm 0.12\ \mu{\rm as}. \quad (11)$$

Here the 5% error is from Table 3 of Adams et al. (2018). For any particular model, one can derive $\theta_* = 2.33 \times 10^{-0.2(I_{\rm S}-17.35)}$. We summarize, θ_*, and the derived $\theta_{\rm E}$ and $\mu_{\rm rel}$ for 2L1S parallax and xallarap models in Table 5.

5. Single-lens Binary-source Model

The total magnification of a 1L2S model is the superposition of the 1L1S magnification of two sources (Hwang et al. 2013):

$$A_\lambda = \frac{A_1 f_{1,\lambda} + A_2 f_{2,\lambda}}{f_{1,\lambda} + f_{2,\lambda}} = \frac{A_1 + q_{f,\lambda} A_2}{1 + q_{f,\lambda}}, \quad (12)$$

$$q_{f,\lambda} = \frac{f_{2,\lambda}}{f_{1,\lambda}}. \quad (13)$$

Here A_λ is total magnification at wavelength λ, and $f_{{\rm i},\lambda}$ is the baseline flux of each source, with $i = 1$ and 2 corresponding to the primary and the secondary sources, respectively. In the following subsections, we consider two cases: a static binary source (including the microlens-parallax effect) and a binary source with the xallarap effect.

5.1. 1L2S Parallax Model

Table 6 lists the parameters of the best-fit 1L2S model (derived using MCMC). It is disfavored by $\Delta\chi^2 = 78$ compared to the best-fit 2L1S xallarap model, which is significant enough to rule out the 1L2S parallax model. The model also has a large parallax value (>1). Moreover, Gaudi (1998) suggested that the 1L2S model can be excluded by the color difference expected for the two sources with different brightness. For the present case, the 1L2S parallax model indicates almost the same color (i.e., $q_{f,V}/q_{f,I} \sim 1$) for the two sources with about a 7.5 mag difference. According to the CMD analysis in Section 4, the second source has a color of $(V-I) = 1.95 \pm 0.12$. Applying the blue boundary of the bulge main-sequence stars derived by Zhang et al. (2023), a source star with $I \sim 24.8$ should be redder than $(V-I) = 2.9$ (see Figure 6). Therefore, the 1L2S parallax model can also be excluded by $\sim 8\sigma$ based on the color argument.

5.2. 1L2S Xallarap Model

We consider a model with a single lens, two luminous sources, and full Keplerian motion of the source components (i.e., xallarap). In this model, the anomaly is produced by the approach of the secondary source to the lens. Such a model has a low a priori probability because the xallarap effect has to produce a significant difference in the observed timescales of the two subevents.

For the MCMC fitting of such a model, one has to start with a model that produces the anomaly at the right time. If one sets the xallarap parameters to some random values and starts MCMC from them, then the exploration of the parameter space will be extremely inefficient: most sets of xallarap parameters will not produce anomaly at the right time. In order to find starting parameters for MCMC, we performed several steps described below.

First, we randomly draw many sets of parameters. We consider two types of xallarap orbits: circular and eccentric. For circular orbits, we use normal distributions for (t_0, u_0, $t_{\rm E}$) with means found in a fit without the anomaly and small dispersions. Then, ξ_P is drawn from a log-uniform distribution from 50 to 500 days, ξ_a is drawn from a log-uniform distribution from 0.01 to 0.5, angles (ξ_i, ξ_Ω, ξ_u) are from uniform distributions, and q_s is log-uniform from 0.001 to 0.5. We fix $t_{0,\xi}$ at HJD′ = 7880 (note that this differs from 2L1S choice). For eccentric orbits, there are two additional parameters: eccentricity of xallarap (ξ_e) drawn from a log-uniform distribution from 0.01 to 1 and argument of periapsis (ξ_ω) drawn from a uniform distribution. After drawing 2×10^8 circular and the same number of eccentric orbits, we select the ones for which the distance between the second source and the lens at HJD′ = 7810.5 was smaller than 0.1 because the second source is much fainter and thus needs to pass very close to the lens to produce a significant anomaly. There were around 26,000 such orbits of each type. Then we calculated χ^2 values for these models without any constraints on fluxes. We selected 100 models with the smallest χ^2 in each case, and for them, we ran the MCMC with only two parameters fitted: the ratio of the source fluxes for the I band, $q_{f,I}$, and the ratio for the V band,

Table 2
Lensing Parameters for 2L1S Parallax Models

Parameters	Close Inner		Close Outer		Wide	
	$u_0 > 0$	$u_0 < 0$	$u_0 > 0$	$u_0 < 0$	$u_0 > 0$	$u_0 < 0$
χ^2/dof	10101.8/10683	10116.7/10683	10107.8/10683	10119.7/10683	**10086.0/10683**	10102.4/10683
t_0	$7879.03^{+0.13}_{-0.16}$	$7879.28^{+0.13}_{-0.46}$	$7879.01^{+0.11}_{-0.14}$	$7878.93^{+0.15}_{-0.15}$	$\mathbf{7878.93^{+0.12}_{-0.12}}$	$7879.15^{+0.14}_{-0.17}$
u_0	$1.22^{+0.02}_{-0.03}$	$-1.21^{+0.05}_{-0.03}$	$1.17^{+0.07}_{-0.12}$	$-1.23^{+0.01}_{-0.01}$	$\mathbf{1.14^{+0.07}_{-0.08}}$	$-1.22^{+0.06}_{-0.02}$
t_E(days)	$31.4^{+0.9}_{-1.3}$	$27.4^{+3.4}_{-0.9}$	$29.7^{+2.0}_{-1.2}$	$32.5^{+0.7}_{-0.8}$	$\mathbf{30.5^{+1.6}_{-1.2}}$	$28.2^{+1.6}_{-0.8}$
ρ (10^{-2})	$0.13^{+0.36}_{-0.05}$	$0.80^{+0.11}_{-0.29}$	$0.67^{+0.08}_{-0.06}$	$0.09^{+0.20}_{-0.05}$	$\mathbf{1.81^{+0.22}_{-0.33}}$	$1.37^{+0.60}_{-0.69}$
$\pi_{E,\ N}$	$0.36^{+0.40}_{-0.23}$	$-2.19^{+1.54}_{-0.24}$	$1.38^{+0.14}_{-0.17}$	$-0.11^{+0.15}_{-0.19}$	$\mathbf{1.19^{+0.14}_{-0.14}}$	$-1.71^{+0.42}_{-0.23}$
$\pi_{E,\ E}$	$0.42^{+0.16}_{-0.08}$	$0.36^{+0.07}_{-0.05}$	$0.86^{+0.07}_{-0.06}$	$0.34^{+0.04}_{-0.03}$	$\mathbf{0.74^{+0.05}_{-0.06}}$	$0.34^{+0.04}_{-0.05}$
$t_{0,pl}$	$7810.6^{+1.6}_{-2.7}$	$7814.0^{+4.7}_{-4.9}$	$7807.4^{+5.1}_{-4.0}$	$7813.8^{+2.0}_{-1.8}$	$\mathbf{7799.5^{+4.7}_{-4.7}}$	$7803.8^{+2.7}_{-2.4}$
$u_{0,pl}$	$-0.09^{+0.11}_{-0.19}$	$1.51^{+0.29}_{-0.85}$	$-1.16^{+0.27}_{-0.22}$	$0.00^{+0.07}_{-0.06}$	$\mathbf{-0.78^{+0.14}_{-0.14}}$	$1.04^{+0.18}_{-0.23}$
$t_{E,\ pl}$ (days)	$1.36^{+0.39}_{-0.14}$	$3.00^{+0.43}_{-1.26}$	$3.02^{+0.45}_{-0.42}$	$1.25^{+0.11}_{-0.07}$	$\mathbf{0.37^{+0.04}_{-0.04}}$	$0.36^{+0.03}_{-0.05}$
ds/dt (yr^{-1})	$0.12^{+0.06}_{-0.03}$	$0.38^{+0.17}_{-0.16}$	$0.31^{+0.17}_{-0.12}$	$0.21^{+0.05}_{-0.05}$	$\mathbf{-0.32^{+1.06}_{-1.12}}$	$-0.27^{+0.67}_{-0.62}$
$d\alpha/dt$ (yr^{-1})	$-0.4^{+0.7}_{-5.9}$	$-44.5^{+45.2}_{-64.9}$	$50.5^{+55.6}_{-44.0}$	$0.2^{+0.3}_{-0.5}$	$\mathbf{-0.1^{+19.0}_{-21.6}}$	$-0.4^{+15.6}_{-18.8}$
I_S	$17.32^{+0.06}_{-0.05}$	$17.34^{+0.11}_{-0.06}$	$17.45^{+0.26}_{-0.14}$	$17.29^{+0.03}_{-0.02}$	$\mathbf{17.51^{+0.18}_{-0.16}}$	$17.32^{+0.12}_{-0.05}$
π_E	$0.55^{+0.40}_{-0.18}$	$2.22^{+0.23}_{-1.43}$	$1.63^{+0.13}_{-0.18}$	$0.38^{+0.09}_{-0.05}$	$\mathbf{1.40^{+0.14}_{-0.14}}$	$1.74^{+0.23}_{-0.39}$
s	$0.356^{+0.007}_{-0.010}$	$0.365^{+0.018}_{-0.020}$	$0.363^{+0.022}_{-0.021}$	$0.368^{+0.009}_{-0.008}$	$\mathbf{2.967^{+0.168}_{-0.187}}$	$3.002^{+0.120}_{-0.132}$
$q(10^{-4})$	$18.64^{+14.52}_{-4.16}$	$121.47^{+36.51}_{-92.09}$	$104.17^{+28.15}_{-26.53}$	$14.71^{+3.24}_{-1.81}$	$\mathbf{1.46^{+0.32}_{-0.28}}$	$1.68^{+0.33}_{-0.53}$
α (deg)	$27.2^{+3.3}_{-5.1}$	$7.7^{+6.1}_{-21.2}$	$0.0^{+5.9}_{-5.3}$	$328.3^{+2.7}_{-2.1}$	$\mathbf{187.6^{+3.3}_{-3.4}}$	$176.4^{+3.9}_{-5.4}$

Note. Bold column indicates the preferred model.

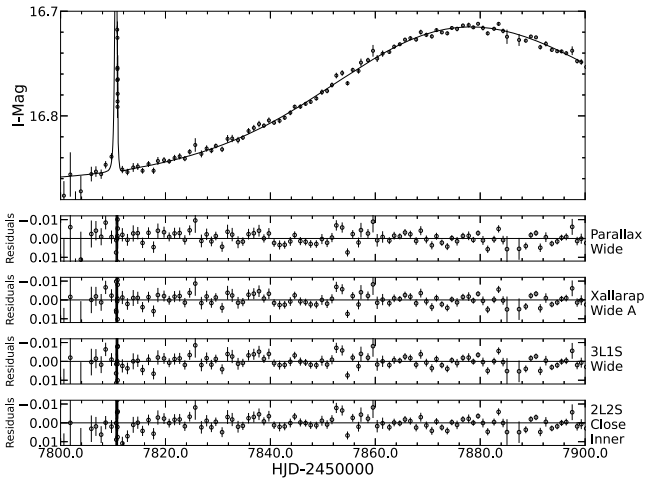

Figure 4. Daily binned data together with the best-fit models of 2L1S parallax, 2L1S xallarap, 3L1S, and 2L2S. All of the four models can remove the long-term residuals shown in Figure 3.

$q_{f,V}$. We further narrowed down the models considered to the ones with χ^2 below a threshold value of 10350, which resulted in 20 circular orbits and 24 eccentric orbits.

The above multistep procedure allows us to go from 4×10^8 randomly drawn sets of parameters to 44 that have light curves resembling the observed one. Importantly, the above procedure is robust and efficient. For each of the above models we then run MCMC with the fitting of all the microlensing parameters: three PSPL ones, five basic xallarap ones (plus two more for eccentric orbits), the mass ratio of the two sources, q_S, and two ratios of source fluxes. In total, there are 11 parameters for circular orbits and 13 for eccentric ones. These MCMC runs include the constraint on the maximum source flux as other models described before (this constraint is not used in calculations presented in the previous paragraph). We found the smallest χ^2 of 10082.1. However, this model is unphysical: $q_S = 0.00399 \pm 0.00063$ points to a planet-to-star mass ratio but the flux ratio $q_{f,I} = 0.094 \pm 0.015$ points to a G or K dwarf as a secondary. The other solutions all have planetary or brown-dwarf mass ratios (i.e., $q_S < 0.03$) and stellar flux ratios ($q_{f,I} > 10^{-3}$).

Some of the models considered have a very close approach of the second source to the lens. Hence, we run another 44 MCMC runs with finite-source effects for the second source. We introduce an additional parameter: ρ_2—the angular size of the second source scaled to θ_E. This increases the number of parameters to 12 (circular orbits) or 14 (eccentric orbits). We assumed a uniform brightness profile and used single-lens finite-source calculations that implement the Gould (1994a) method. The lowest χ^2 of these runs is 10062.6; however, all source mass ratios are still in the planetary range while flux ratios are in the stellar range. Moreover, the color of the secondary source is also inconsistent with the color of bulge main-sequence stars. We conclude that none of the 1L2S with xallarap models that fit the data well are physical.

6. Physical Parameters and Model Preference

From the 2L1S analysis, we obtain six parallax models and eight xallarap models. In this section, we estimate physical parameters of lenses in these models by conducting a Bayesian analysis based on the Galactic model, which also can be used to infer the preferred model (e.g., OGLE-2017-BLG-1806, Zang et al. 2023). The Galactic model we adopt is the same as the model used by Yang et al. (2021) and assumes that the planet occurrence rate does not depend on host star properties. We note that Gaia (Gaia Collaboration et al. 2016, 2018) reported a proper motion measurement for the object at the event position. However, we do not adopt this measurement in the Bayesian analysis because Gaia did not resolve the nearby field star that is 0.″5 away from the source, the event could contain a blend, and the Gaia goodness-of-fit parameter RUWE has a high value: 1.65.

Table 3
Lensing Parameters for Close ($s < 1$) Xallarap Models

	Close Inner		Close Outer		
	A	B	A	B	C
χ^2/dof	10080.2/10682	10074.7/10682	10078.1/10682	10084.6/10682	10084.9/10682
t_0	7882.2 ± 0.5	$7881.1^{+2.6}_{-7.3}$	7881.2 ± 0.8	$7883.0^{+1.5}_{-2.3}$	$7883.7^{+1.0}_{-1.7}$
u_0	$1.20^{+0.05}_{-0.08}$	1.57 ± 0.23	1.03 ± 0.08	1.21 ± 0.16	$1.13^{+0.17}_{-0.13}$
t_E(days)	$32.0^{+1.5}_{-1.0}$	39.9 ± 2.8	$28.0^{+1.5}_{-1.2}$	32.0 ± 2.3	31.3 ± 1.9
$\rho(10^{-2})$	0.078 ± 0.028	0.088 ± 0.041	$0.044^{+0.047}_{-0.031}$	$0.033^{+0.031}_{-0.024}$	$0.336^{+0.085}_{-0.062}$
$t_{0,pl}$	7813.5 ± 0.3	$7815.9^{+1.1}_{-0.9}$	7808.2 ± 0.3	7807.1 ± 0.8	7807.5 ± 0.6
$u_{0,pl}$	$0.155^{+0.019}_{-0.016}$	0.134 ± 0.018	$-0.255^{+0.026}_{-0.037}$	-0.245 ± 0.023	-0.246 ± 0.024
$t_{E,pl}$ (days)	1.06 ± 0.10	1.48 ± 0.15	1.34 ± 0.13	$1.56^{+0.21}_{-0.15}$	1.53 ± 0.16
ξ_P (days)	77^{+16}_{-8}	150^{+36}_{-14}	101^{+6}_{-5}	172^{+21}_{-15}	166 ± 16
ξ_a	$0.049^{+0.013}_{-0.009}$	$0.320^{+0.120}_{-0.070}$	0.233 ± 0.053	$0.358^{+0.093}_{-0.077}$	0.325 ± 0.081
ξ_Ω (deg)	295 ± 11	136^{+8}_{-17}	96^{+3}_{-3}	135 ± 6	313 ± 7
ξ_i (deg)	112^{+10}_{-18}	129^{+5}_{-4}	117^{+3}_{-4}	115 ± 8	111^{+7}_{-9}
ξ_u (deg)	167^{+41}_{-30}	34^{+21}_{-15}	77 ± 14	111 ± 16	291 ± 13
I_S	$18.20^{+0.17}_{-0.18}$	$17.98^{+0.24}_{-0.22}$	$18.13^{+0.19}_{-0.22}$	$17.96^{+0.24}_{-0.22}$	$18.00^{+0.27}_{-0.25}$
s	$0.347^{+0.014}_{-0.009}$	$0.365^{+0.026}_{-0.019}$	$0.327^{+0.013}_{-0.008}$	$0.343^{+0.018}_{-0.015}$	0.341 ± 0.016
$q(10^{-4})$	10.9 ± 2.0	$13.7^{+2.9}_{-2.3}$	$22.3^{+5.5}_{-3.6}$	$24.1^{+3.5}_{-2.8}$	23.7 ± 3.8
α (deg)	$32.15^{+0.57}_{-0.73}$	$46.0^{+6.4}_{-4.1}$	16.6 ± 1.7	22.1 ± 3.7	20.3 ± 3.1

Table 4
Lensing Parameters for Wide ($s > 1$) Xallarap Models

	Wide		
	A	B	C
χ^2/dof	**10071.7/10682**	10074.2/10682	10077.9/10682
t_0	$\mathbf{7881.63}^{+2.30}_{-4.87}$	$7882.10^{+0.72}_{-0.91}$	$7882.47^{+0.47}_{-0.59}$
u_0	$\mathbf{1.34 \pm 0.28}$	$0.92^{+0.25}_{-0.19}$	$1.08^{+0.14}_{-0.21}$
t_E(days)	$\mathbf{45.58 \pm 8.40}$	$33.45^{+3.98}_{-3.06}$	$32.51^{+3.72}_{-2.23}$
ρ (10^{-2})	$\mathbf{0.74}^{+0.42}_{-0.27}$	$0.66^{+0.38}_{-0.56}$	0.60 ± 0.43
$t_{0,pl}$	$\mathbf{7810.56}^{+0.11}_{-0.17}$	$7810.61^{+0.06}_{-0.11}$	$7810.52^{+0.11}_{-0.09}$
$u_{0,pl}$	$\mathbf{-0.005}^{+0.011}_{-0.004}$	$0.002^{+0.002}_{-0.010}$	$0.001^{+0.004}_{-0.009}$
$t_{E,pl}$ (days)	$\mathbf{0.45 \pm 0.13}$	$0.25^{+0.05}_{-0.03}$	0.25 ± 0.03
ξ_P (days)	$\mathbf{155.5}^{+22.7}_{-12.0}$	93.8 ± 10.6	87.0 ± 8.8
ξ_a	$\mathbf{0.326}^{+0.096}_{-0.060}$	0.132 ± 0.059	$0.085^{+0.040}_{-0.022}$
ξ_Ω (deg)	$\mathbf{143.0}^{+6.5}_{-9.4}$	$279.7^{+9.5}_{-4.1}$	$104.0^{+9.0}_{-5.9}$
ξ_i (deg)	$\mathbf{132.4 \pm 3.7}$	$112.5^{+4.8}_{-8.3}$	113.9 ± 6.9
ξ_u (deg)	$\mathbf{60.6 \pm 20.0}$	$236.8^{+22.5}_{-38.4}$	29.9 ± 29.0
I_S	$\mathbf{17.35}^{+0.50}_{-0.18}$	$17.56^{+0.52}_{-0.23}$	$17.78^{+0.44}_{-0.35}$
s	$\mathbf{2.45}^{+0.40}_{-0.30}$	2.70 ± 0.25	$2.82^{+0.19}_{-0.26}$
q (10^{-4})	$\mathbf{0.98}^{+0.31}_{-0.21}$	0.55 ± 0.14	0.57 ± 0.11
α (deg)	$\mathbf{220.6 \pm 3.9}$	$203.1^{+3.3}_{-2.6}$	$206.2^{+1.5}_{-2.1}$

Note. Bold column indicates the preferred model.

We create a sample of 10^8 simulated events. For each simulated event i of solution k, we weigh it by

$$w_{\mathrm{Gal},i,k} = \Gamma_{i,k} \times p_{i,k}(t_E) p_{i,k}(\theta_E) p_{i,k}(\pi_E), \quad (14)$$

where $\Gamma_{i,k} = \theta_{E,i,k} \times \mu_{\mathrm{rel},i,k}$ is the microlensing event rate, $_{pi,k}(t_E)_{pi,k}(\theta_E)$ and $_{pi,k}(\pi_E)$ are the likelihood distributions of $t_{E,i,k}$, $\theta_{E,i,k}$ and $\pi_{E,i,k}$ from light-curve and CMD analysis.

Table 7 shows the resulting posterior distributions of the host mass, M_1, the planet mass, M_{planet}, the lens distance, D_L, the projected planet–host separation, $a_{\perp,\mathrm{planet}}$, and the lens–source relative proper motion, μ_{rel}. Table 7 also presents the $\Delta\chi^2$ between different models based on the relative probability from the Galactic model and the light-curve analysis. The 2L1S xallarap model "Wide A" has the highest probability, and the six 2L1S parallax models are disfavored by $\Delta\chi^2 \geqslant 34.8$. For four of the 2L1S parallax models, "Close Inner ($u_0 < 0$)," "Close Outer ($u_0 > 0$)," "Wide ($u_0 > 0$)," and "Wide ($u_0 < 0$)," the host star is a median- or low-mass brown dwarf located in the Galactic disk and thus the lens number density and Galactic model likelihood are low. For the other two 2L1S parallax models, "Close Inner ($u_0 > 0$)" and "Close Outer ($u_0 < 0$)," although their Galactic model likelihoods are slightly low, they are disfavored by $\Delta\chi^2 \geqslant 30.1$ from the light-curve analysis. Therefore, we only adopt the xallarap models as our surviving models.[16]

For the eight 2L1S xallarap models, all are within $5\sigma$and probably have M or K dwarf hosts. We further check whether their source systems are physically reasonable. We calculate the source semimajor axis by

$$a_S = \xi_a \theta_E D_S, \quad (15)$$

where D_S is the source distance and we use its distribution from the Bayesian analysis above. Then, we derive the mass and separation for the source companion by Kepler's third law. Table 8 lists the information for the source companion, including the mass, M_{com}, the 3σ lower limit for M_{com}, the separation from the source, a_{tot}. Three models, "Close Inner B," "Close Outer A," and "Close Outer B," probably require an intermediate-mass black hole source companion, so we exclude them. For the remaining five models, three have a wide topology with projected planet–host separations of $\sim$6 au and planetary masses between super-Earth mass and Neptune mass,

[16] The xallarap models have only one more parameter than the parallax models, so even if we conduct the model selection using Akaike's information criterion or the Bayesian information criterion, the parallax models are still disfavored by $>5\sigma$ (i.e., $\Delta\chi^2 > 25$).

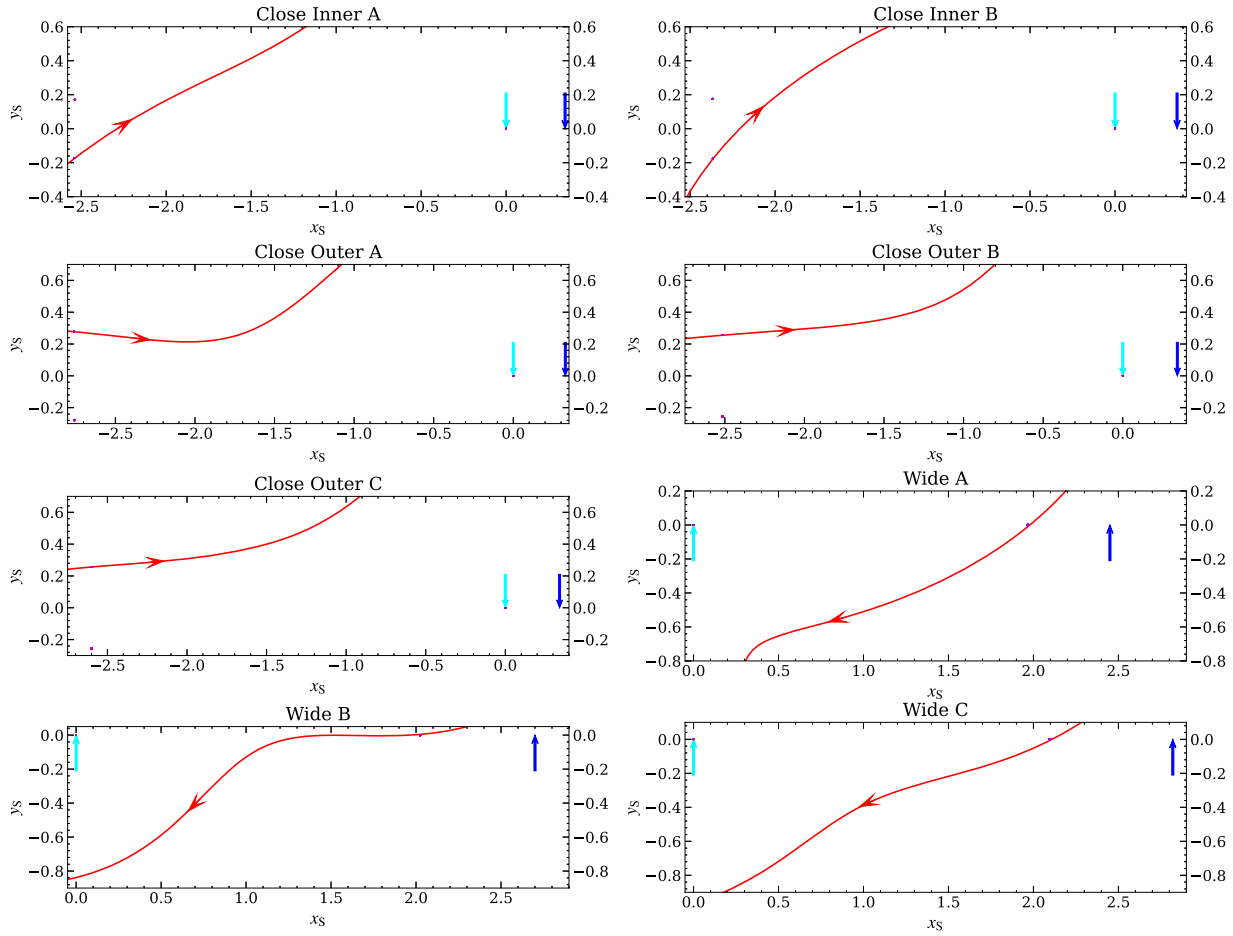

Figure 5. Source trajectories of the 2L1S xallarap models. The symbols are similar to those in Figure 2. Their parameters are given in Tables 3 and 4. The "Close Outer B" and "Close Outer C" models have almost the same trajectories, but their source radii are different.

and two have a close topology with projected planet–host separations of ∼1 au and the planetary masses of ∼1 Jovian mass. The relative lens–source proper motion of the "Close Inner A" model is significantly higher than the other four solutions, with $\mu_{\rm rel} \sim 13$ mas yr^{-1}. The brightness contrast for the source and the lens is ∼100 in the near-infrared band, so it probably requires a separation of ∼100 mas to resolve them by the current high-angular resolution instruments. Therefore, the "Close Inner A" model may be tested in 2025 or earlier. The other four solutions, "Wide A," "Wide B," "Wide C," and "Close Outer C" cannot be distinguished by high-angular resolution imaging due to the similar $\mu_{\rm rel}$.

7. Discussion: Four-body Models

We have followed the "standard" light-curve analysis for a microlensing planetary event. That is, we have fitted the observed data with three-body models (2L1S and 1L2S) and tried high-order effects (the parallax, lens orbital motion, and xallarap effects) to fit out the long-term residuals from the static models. We have found that the 2L1S xallarap models fit the observed data well (Figure 4), and the resulting lens physical parameters based on the Bayesian analysis are physically reasonable (Table 7). However, we are still wondering whether the long-term residuals can be fitted by adding a fourth body instead of high-order effects. Therefore, we pursue four-body models in Sections 7.1 and 7.2 and discuss the implications in Section 7.3.

7.1. Triple-lens Single-source Model

First, we add an additional lens component to the static 2L1S model to fit the long-term residuals, i.e., the triple-lens single-source (3L1S) model. Relative to the static 2L1S model, the 3L1S models have three additional parameters, (s_3, q_3, ψ), to describe the third body, M_3. These are the M_1–M_3 separation scaled to $\theta_{\rm E}$, the mass ratio of M_3 relative to M_1, and the orientation angle of M_3 with respect to the M_1–M_2 axis as seen from M_1. To avoid confusion, for the 3L1S analysis we designate s_2 and q_2 for the separation and mass ratio of M_2 to M_1, respectively.

We adopt the binary superposition method (Han et al. 2001; Han 2005) to search for the 3L1S models (see the Appendix of Kuang et al. 2022 for the detailed procedures). We adopt the contour-integration code (Kuang et al. 2021) to calculate the 3L1S magnification. The contour-integration-based algorithm developed by Kuang et al. (2021) can deal with self-intersecting caustic crossings. The false solutions from the tenth-order polynomial are used to help obtain the image boundaries, and Figure 9 of Kuang et al. (2021) exhibits an example magnification map and a comparison with the ray-shooting-based method. In addition, for the present case, only distant (planetary) caustic is closely approached by the source, and our final models show separations significantly different

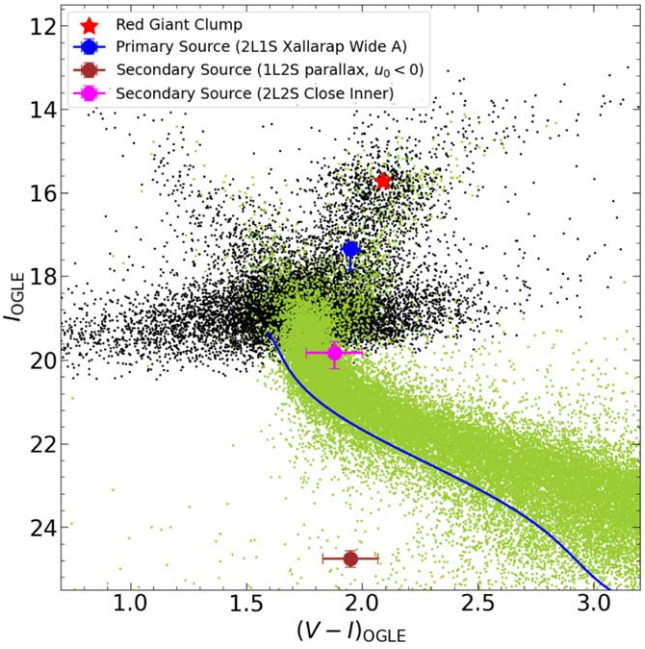

Figure 6. CMD (black points) within 120″ of OGLE-2017-BLG-0448 using the OGLE-III star catalog (Szymański et al. 2011). The red asterisk indicates the centroid of the red giant clump. The blue line indicates the blue boundary of the bulge main-sequence stars (Zhang et al. 2023). The yellow-green points show the HST CMD of Holtzman et al. (1998). The blue dot represents the source position for the 2L1S xallarap "Wide A" model. For other models, the source color is the same and the source brightness depends on particular models (Tables 3 and 4). The brown and magenta dots show the secondary sources for the 1L2S parallax ($u_0 < 0$) and 2L2S "Close Inner" models.

Table 5
θ_*, θ_E and μ_{rel} for the 2L1S Models

Model	$I_{S,0}$	θ_* (μas)	θ_E (mas)	μ_{rel} (mas yr^{-1})
2L1S Parallax				
Close Inner ($u_0 > 0$)	$16.30^{+0.07}_{-0.06}$	$2.13^{+0.09}_{-0.09}$	>0.33	>4.1
Close Inner ($u_0 < 0$)	$16.32^{+0.12}_{-0.07}$	$2.11^{+0.11}_{-0.12}$	$0.26^{+0.16}_{-0.05}$	$3.48^{+1.44}_{-0.48}$
Close Outer ($u_0 > 0$)	$16.43^{+0.26}_{-0.14}$	$2.00^{+0.15}_{-0.23}$	$0.29^{+0.04}_{-0.04}$	$2.59^{+0.62}_{-0.59}$
Close Outer ($u_0 < 0$)	$16.27^{+0.05}_{-0.05}$	$2.16^{+0.08}_{-0.08}$	>0.44	>5.1
Wide ($u_0 > 0$)	$16.49^{+0.18}_{-0.16}$	$1.95^{+0.15}_{-0.16}$	$0.11^{+0.02}_{-0.01}$	$1.28^{+0.23}_{-0.12}$
Wide ($u_0 < 0$)	$16.30^{+0.13}_{-0.06}$	$2.13^{+0.10}_{-0.14}$	$0.15^{+0.16}_{-0.05}$	$1.90^{+1.84}_{-0.54}$
2L1S Xallarap				
Close Inner A	$16.96^{+0.17}_{-0.18}$	$1.57^{+0.15}_{-0.14}$	>0.90	>10.4
Close Inner B	$16.74^{+0.24}_{-0.22}$	$1.74^{+0.20}_{-0.20}$	>0.67	>6.2
Close Outer A	$16.89^{+0.19}_{-0.22}$	$1.62^{+0.19}_{-0.16}$	>0.46	>6.0
Close Outer B	$16.72^{+0.24}_{-0.22}$	$1.76^{+0.20}_{-0.20}$	>1.36	>12.4
Close Outer C	$16.76^{+0.27}_{-0.25}$	$1.73^{+0.23}_{-0.23}$	>0.28	>3.3
Wide A	$16.11^{+0.50}_{-0.18}$	$2.33^{+0.23}_{-0.50}$	>0.09	>0.72
Wide B	$16.32^{+0.52}_{-0.23}$	$2.11^{+0.26}_{-0.47}$	>0.11	>1.2
Wide C	$16.46^{+0.44}_{-0.35}$	$1.91^{+0.35}_{-0.36}$	>0.11	>1.2

Note. The lower limits for θ_E and μ_{rel} are at 3σ.

from unity and for the self-crossing configurations. Hence, the algorithm used for 3L1S magnification calculations is appropriate for the present case.

We exclude the data during $7809.4 < HJD' < 7811$ (i.e., the signature of the planet, M_2) and conduct a 2L1S grid search, which consists of 41 values of $\log s_3$ equally spaced between -1.00 and 1.00, 21 values of $\log q_3$ equally spaced between -2.0 and 0.0, and 24 values equally spaced between

Table 6
Lensing Parameters for 1L2S Parallax Models

Parameters	$u_1 > 0$	$u_1 < 0$
χ^2/dof	10188.4/10684	10149.6/10684
$t_{0,1}$	$7878.35^{+0.24}_{-0.23}$	$7877.63^{+0.39}_{-0.44}$
$u_{0,1}$	$1.195^{+0.017}_{-0.031}$	$-1.200^{+0.053}_{-0.024}$
t_E(days)	$45.2^{+1.2}_{-1.4}$	$53.6^{+3.4}_{-3.6}$
$t_{0,2}$	$7818.8^{+1.4}_{-1.8}$	$7824.8^{+4.8}_{-6.0}$
$u_{0,2}$	$-0.877^{+0.041}_{-0.028}$	$1.252^{+0.067}_{-0.090}$
ρ_2 (10^{-2})	$2.43^{+0.24}_{-0.19}$	$3.34^{+0.50}_{-0.52}$
$q_{f,I}$ (10^{-3})	$0.76^{+0.07}_{-0.06}$	$1.08^{+0.15}_{-0.12}$
$q_{f,V}$ (10^{-3})	$0.76^{+0.11}_{-0.09}$	$1.07^{+0.17}_{-0.15}$
$\pi_{E,N}$	$-1.389^{+0.064}_{-0.042}$	$2.042^{+0.114}_{-0.156}$
$\pi_{E,E}$	$-0.388^{+0.064}_{-0.048}$	$-0.282^{+0.155}_{-0.115}$
$I_{S,total}$	$17.30^{+0.06}_{-0.03}$	$17.33^{+0.11}_{-0.05}$
$q_{f,V}/q_{f,I}$	$1.00^{+0.12}_{-0.10}$	$0.99^{+0.11}_{-0.11}$

Note. $I_{S,total}$ is derived from the total fluxes of the two sources.

$0° \leqslant \psi < 360°$. We fix $\rho = 0$ because the long-term residuals show no caustic-crossing features. We use MCMC to search for the minimum χ^2 and allow (t_0, u_0, t_E, ψ) to vary. We obtain three local minima on the ($\log s_3$, $\log q_3$) plane, with ($\log s_3$, $\log q_3$) = (-0.5, 0.0), (-0.15, -0.7), and (0.65, -0.8), respectively. We then refine the three local minima with the MCMC method by setting all parameters as free, and the first local minimum is favored by $\Delta\chi^2 = 10$ and $\Delta\chi^2 = 5$ compared with the second and third local minima, respectively. The purpose of the 3L1S modeling is to investigate whether a 3L1S model can fit the observed data instead of finding all of the models, so we only adopt the parameters of the first local minimum for the binary superposition method. Combining it with the 2L1S static parameters in Table 1, we also find three models, which are labeled as "3L1S Close Outer," "3L1S Close Inner" and "3L1S Wide."[17] Figure 7 shows the caustics and source trajectories of these models, and their parameters are presented in Table 9. We also conduct a Bayesian analysis following the procedure of Section 6, and the only exception is that we first estimate the primary lens with $t_E$and θ_E by scaling by a factor of $\sqrt{1 + q_2 + q_3}$ smaller than the values from the 3L1S models. Table 7 shows the Bayesian results.

Compared to the best 2L1S xallarap model ("Wide A"), the "3L1S Close Outer" model is excluded by $\Delta\chi^2 = 50.7$ from the light-curve analysis. For the "3L1S Close Inner" model, it is disfavored by both the light-curve analysis (11.3) and the Galactic model likelihood (10.8). The Bayesian analysis suggests a nearby system with two M dwarfs, with an estimated brightness of $I \sim 17.5$ mag, which is significantly brighter than the allowed blended flux, so we can also exclude the "3L1S Close Inner" model. However, the best-fit 3L1S model, the "3L1S Wide" model, is only disfavored relative to the 2L1S xallarap model "Wide A" by $\Delta\chi^2 = 6.2$, so we cannot distinguish between the 2L1S xallarap model and the 3L1S model.

[17] If one assumes circular orbits with the ratio of radii equal to the ratio of observed projected separations, then the two "Close" solutions are dynamically unstable according to conditions presented by Holman & Wiegert (1999).

Table 7
Physical Parameters from a Bayesian Analysis and the $\Delta\chi^2$ from Various Weighting Approaches

	Physical Parameters							$\Delta\chi^2$		
Units	M_1 ($M_\odot$)	$M_{\rm planet}$ ($M_\oplus$)	$D_{\rm L}$ (kpc)	$a_{\perp,{\rm planet}}$ (au)	$\mu_{\rm rel}$ (mas yr^{-1})	M_3 ($M_\odot$)	$a_{\perp,3}$ (au)	Gal.Mod.	Light Curve	Total
2L1S Parallax										
Close Inner ($u_0 > 0$)	$0.15^{+0.06}_{-0.05}$	$86.1^{+68.0}_{-49.6}$	$3.69^{+0.74}_{-0.84}$	$0.57^{+0.11}_{-0.11}$	$5.6^{+1.2}_{-0.8}$	⋯	⋯	6.2	30.1	34.8
Close Inner ($u_0 < 0$)	$0.065^{+0.024}_{-0.021}$	236^{+211}_{-131}	$3.94^{+0.62}_{-1.17}$	$0.39^{+0.07}_{-0.09}$	$4.1^{+1.6}_{-0.7}$	⋯	⋯	15.7	45.0	59.2
Close Outer ($u_0 > 0$)	$0.021^{+0.004}_{-0.002}$	$69.8^{+5.9}_{-5.5}$	$1.94^{+0.07}_{-0.44}$	$0.19^{+0.01}_{-0.02}$	$4.6^{+1.2}_{-0.2}$	⋯	⋯	19.4	36.1	54.0
Close Outer ($u_0 < 0$)	$0.19^{+0.04}_{-0.04}$	$93.3^{+30.4}_{-20.8}$	$3.39^{+0.46}_{-0.42}$	$0.66^{+0.07}_{-0.07}$	$6.6^{+1.1}_{-0.7}$	⋯	⋯	6.5	48.0	53.0
Wide ($u_0 > 0$)	$0.015^{+0.008}_{-0.002}$	$0.84^{+0.28}_{-0.22}$	$3.06^{+0.40}_{-0.80}$	$1.53^{+0.11}_{-0.23}$	$2.7^{+1.3}_{-0.6}$	⋯	⋯	23.3	14.3	36.1
Wide ($u_0 < 0$)	$0.048^{+0.034}_{-0.021}$	$2.56^{+2.07}_{-1.11}$	$4.92^{+2.04}_{-1.60}$	$2.72^{+0.96}_{-0.76}$	$2.7^{+2.0}_{-0.9}$	⋯	⋯	16.0	30.7	45.2
2L1S Xallarap										
Close Inner A	$0.52^{+0.44}_{-0.27}$	190^{+155}_{-101}	$2.25^{+1.89}_{-1.53}$	$0.87^{+0.52}_{-0.44}$	$12.8^{+4.5}_{-2.8}$	⋯	⋯	8.3	8.5	15.3
Close Inner B	$0.66^{+0.39}_{-0.32}$	294^{+187}_{-144}	$3.86^{+1.66}_{-2.11}$	$1.19^{+0.37}_{-0.48}$	$7.9^{+3.9}_{-1.6}$	⋯	⋯	5.8	3.0	7.3
Close Outer A	$0.66^{+0.37}_{-0.34}$	476^{+297}_{-248}	$6.46^{+1.25}_{-2.36}$	$1.03^{+0.22}_{-0.28}$	$6.6^{+2.0}_{-1.1}$	⋯	⋯	2.8	6.4	7.7
Close Outer B	$0.41^{+0.27}_{-0.18}$	330^{+228}_{-144}	$0.68^{+0.61}_{-0.28}$	$0.49^{+0.27}_{-0.18}$	$18.8^{+9.0}_{-4.8}$	⋯	⋯	10.6	12.9	22.0
Close Outer C	$0.65^{+0.36}_{-0.32}$	504^{+304}_{-255}	$6.91^{+1.03}_{-2.08}$	$1.03^{+0.25}_{-0.26}$	$5.5^{+1.5}_{-1.2}$	⋯	⋯	0.0	13.2	11.7
Wide A	$0.50^{+0.38}_{-0.29}$	$15.6^{+13.8}_{-9.3}$	$7.53^{+0.87}_{-1.54}$	$5.75^{+2.39}_{-2.00}$	$3.2^{+1.6}_{-1.1}$	⋯	⋯	1.5	0.0	0.0
Wide B	$0.43^{+0.37}_{-0.25}$	$6.98^{+8.60}_{-4.61}$	$7.66^{+0.82}_{-1.26}$	$5.55^{+2.31}_{-1.73}$	$3.2^{+1.5}_{-1.0}$	⋯	⋯	0.7	2.5	1.7
Wide C	$0.45^{+0.37}_{-0.26}$	$8.35^{+7.36}_{-4.92}$	$7.62^{+0.83}_{-1.36}$	$6.11^{+2.32}_{-2.00}$	$3.5^{+1.4}_{-1.1}$	⋯	⋯	0.2	6.2	4.9
3L1S										
Close Inner	$0.24^{+0.11}_{-0.09}$	171^{+92}_{-64}	$0.45^{+0.21}_{-0.16}$	$0.40^{+0.13}_{-0.14}$	$27.9^{+8.5}_{-7.0}$	$0.21^{+0.09}_{-0.08}$	$0.29^{+0.09}_{-0.10}$	12.3	11.3	22.1
Close Outer	$0.68^{+0.37}_{-0.35}$	783^{+458}_{-401}	$6.22^{+1.17}_{-1.79}$	$1.50^{+0.29}_{-0.40}$	$8.7^{+1.2}_{-1.0}$	$0.48^{+0.27}_{-0.24}$	$1.04^{+0.20}_{-0.28}$	0.8	50.7	50.0
Wide	$0.32^{+0.42}_{-0.21}$	$5.20^{+6.86}_{-3.39}$	$7.69^{+0.83}_{-1.29}$	$4.65^{+3.50}_{-1.59}$	$3.3^{+2.9}_{-1.3}$	$0.23^{+0.31}_{-0.15}$	$0.54^{+0.41}_{-0.19}$	1.8	5.9	6.2
2L2S										
Close Inner	$0.67^{+0.40}_{-0.33}$	299^{+186}_{-150}	$5.06^{+1.47}_{-1.55}$	$1.15^{+0.29}_{-0.34}$	$8.1^{+0.9}_{-0.7}$	⋯	⋯	3.4	18.2	20.1
Close Outer	$0.69^{+0.39}_{-0.35}$	707^{+426}_{-366}	$5.58^{+1.43}_{-1.70}$	$1.08^{+0.25}_{-0.32}$	$7.1^{+0.8}_{-0.7}$	⋯	⋯	3.1	45.0	46.6
Wide	$0.32^{+0.35}_{-0.18}$	$7.28^{+8.35}_{-4.12}$	$7.79^{+0.81}_{-1.08}$	$5.53^{+1.69}_{-1.19}$	$2.6^{+0.8}_{-0.5}$	⋯	⋯	2.0	21.3	21.8

Note. Gal.Mod. represents the relative probability from the Galactic model, for which the $\Delta\chi^2$ is derived by $-2\ln$(Gal.Mod.). The $\Delta\chi^2$ of light-curve analysis are from Tables 2, 3, 4, 9, and 10.

Table 8
Source Companions for the 2L1S Xallarap Models

	$M_{\rm comp}(M_\odot)$	$M_{\rm comp,limit}(M_\odot)$	$a_{\rm tot}$ (au)
Close Inner A	$13.6^{+28.5}_{-9.1}$	>1.0	$0.86^{+0.36}_{-0.22}$
Close Inner B	1284^{+4012}_{-1012}	>3.7	$5.65^{+3.37}_{-2.28}$
Close Outer A	1018^{+2805}_{-797}	>4.6	$4.28^{+2.37}_{-1.71}$
Close Outer B	2063^{+4037}_{-1496}	>33	$7.70^{+3.26}_{-2.69}$
Close Outer C	$4.8^{+5.7}_{-2.6}$	>0.39	$1.62^{+0.41}_{-0.30}$
Wide A	$4.4^{+15.6}_{-3.1}$	>0.28	$0.99^{+0.57}_{-0.24}$
Wide B	$1.2^{+4.7}_{-0.8}$	>0.01	$0.53^{+0.23}_{-0.08}$
Wide C	$0.8^{+3.6}_{-0.5}$	>0.02	$0.48^{+0.20}_{-0.06}$

Note. $M_{\rm comp,\ limit}$ is the 3σ lower limit for $M_{\rm comp}$.

7.2. Binary-lens Binary-source Model

Second, we add a source companion to the static 2L1S model to fit out the long-term residuals, and now the model is a binary-lens binary-source model (2L2S). Different from the 2L1S xallarap model, here we consider the flux and magnification from the source companion but ignore the orbital motions of the two sources.

Similar to the 1L2S model, the total magnification of a 2L2S model is the superposition of the 2L1S magnification of the two sources. The 2L2S model has an identical definition of the total magnification A_λ and the flux ratio $q_{f,\lambda}$ as in Equations (12) and (13). To obtain an initial guess for the secondary source, we first fit a 1L2S model with the planetary anomaly ($7809.4 < {\rm HJD}' < 7811$) removed. There are no useful constraints on the scaled radius for the secondary source, ρ_2, so we adopt a point-like secondary source. Then, we add the binary-lens parameters (ρ, $t_{0,\rm pl}$, $u_{0,\rm pl}$, and $t_{\rm E,\ pl}$) of the 2L1S static models and search for the best-fit models using the MCMC. We also conduct a Bayesian analysis for the 2L2S models.

Table 10 presents the parameters from the MCMC, and Table 7 shows the Bayesian results. The Inner and Outer models for the Wide topology also merge into one. Compared to the best 2L1S xallarap model ("Wide A"), the "2L2S Close Outer" model can be ruled out by $\Delta\chi^2 = 45.0$. Both the "2L2S Close Inner" and "2L2S Wide" models are disfavored by $\Delta\chi^2 \sim 20$, indicating that they are significantly disfavored but cannot be fully excluded.

The two sources have similar colors, i.e., $q_{f,V}/q_{f,I} \sim 1$. Different from the very low flux ratio in the I band for the 1L2S models, $q_{f,I} \sim 10^{-3}$, the secondary source is only $\lesssim$2.5 mag fainter than the primary source. According to the CMD (Figure 6), the putative secondary source is a typical bulge main-sequence star or subgiant, so we cannot rule out the 2L2S models by the color argument.

7.3. Implications: Dimension-degeneracy Disasters

Together with the 3L1S and 2L2S models, we have respectively investigated four effects to fit out the long-term

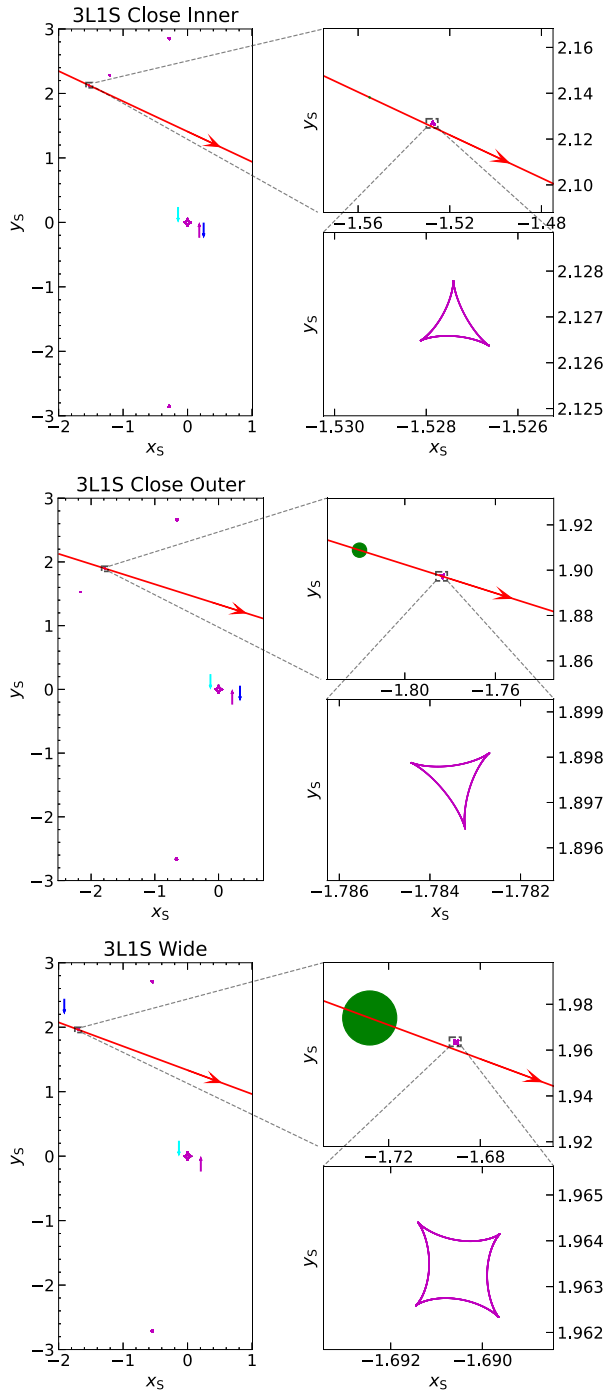

Figure 7. Caustic geometries of the 3L1S models. The locations of the host star, the planet, and the third body are indicated by cyan, blue, and magenta arrows, respectively.

residuals. They are parallax, xallarap, an additional lens, and an additional source. From the perspective of light-curve analysis alone, the four effects all can fit the light curve well and we cannot exclude any effect. To the best of our knowledge, before this case, only Yang et al. (2024) respectively explored all four of these effects for a single event. In that case, two of the effects (parallax or adding a source) were excluded because they could not fit the light curve ($\Delta\chi^2 \gtrsim 50$). Therefore, for the first time, a severe degeneracy between the four effects was found in a real case. In addition, Yang et al. (2024) investigated

Table 9
Lensing Parameters for the 3L1S Models

Parameters	Close Inner	Close Outer	Wide
χ^2/dof	10083.0/10684	10122.4/10684	**10077.6/10684**
t_0	$7884.59^{+0.17}_{-0.15}$	$7884.31^{+0.27}_{-0.32}$	$\mathbf{7884.47^{+0.37}_{-0.38}}$
u_0	$1.288^{+0.012}_{-0.018}$	$1.246^{+0.036}_{-0.051}$	$\mathbf{1.276^{+0.068}_{-0.052}}$
t_E (days)	$31.90^{+0.29}_{-0.24}$	$32.79^{+0.93}_{-0.64}$	$\mathbf{32.22^{+1.03}_{-0.80}}$
ρ (10^{-2})	$0.033^{+0.014}_{-0.009}$	$0.316^{+0.027}_{-0.030}$	$\mathbf{1.159^{+0.049}_{-0.078}}$
s_2	$0.4530^{+0.0051}_{-0.0038}$	$0.4943^{+0.0102}_{-0.0071}$	$\mathbf{2.8838^{+0.0729}_{-0.0856}}$
q_2 (10^{-4})	$25.26^{+3.54}_{-3.59}$	$32.83^{+5.36}_{-5.13}$	$\mathbf{0.49^{+0.07}_{-0.05}}$
α (deg)	$-25.39^{+0.44}_{-0.58}$	$-16.65^{+3.26}_{-3.39}$	$\mathbf{-22.22^{+4.18}_{-4.13}}$
s_3	$0.3335^{+0.0049}_{-0.0043}$	$0.3454^{+0.0077}_{-0.0062}$	$\mathbf{0.3364^{+0.0077}_{-0.0093}}$
q_3	$0.809^{+0.038}_{-0.034}$	$0.551^{+0.092}_{-0.080}$	$\mathbf{0.727^{+0.144}_{-0.094}}$
ψ (deg)	$-29.02^{+0.54}_{-0.62}$	$-18.34^{+1.80}_{-2.02}$	$\mathbf{126.40^{+3.97}_{-4.30}}$
I_S	$17.270^{+0.035}_{-0.023}$	$17.361^{+0.100}_{-0.070}$	$\mathbf{17.294^{+0.109}_{-0.126}}$

Note. Bold column indicates the preferred model.

Table 10
Lensing Parameters for the 2L2S Models

Parameters	Close Inner	Close Outer	Wide
χ^2/dof	**10089.9/10682**	10116.7/10682	10093.0/10682
$t_{0,1}$	$\mathbf{7884.82^{+0.72}_{-0.74}}$	$7888.18^{+0.49}_{-0.59}$	$7892.27^{+1.70}_{-1.96}$
$u_{0,1}$	$\mathbf{1.244^{+0.048}_{-0.070}}$	$1.317^{+0.020}_{-0.033}$	$1.292^{+0.046}_{-0.079}$
t_E(days)	$\mathbf{32.19^{+1.06}_{-0.75}}$	$30.38^{+0.52}_{-0.49}$	$30.17^{+1.42}_{-0.68}$
$t_{0,2}$	$\mathbf{7866.0^{+1.0}_{-1.1}}$	$7867.7^{+0.7}_{-0.6}$	$7870.2^{+0.9}_{-1.1}$
$u_{0,2}$	$\mathbf{0.687^{+0.051}_{-0.077}}$	$0.851^{+0.030}_{-0.033}$	$0.974^{+0.057}_{-0.082}$
ρ_1 (10^{-2})	$\mathbf{0.100^{+0.183}_{-0.033}}$	$0.038^{+0.306}_{-0.024}$	$0.954^{+0.159}_{-0.722}$
$q_{f,I}$	$\mathbf{0.105^{+0.029}_{-0.031}}$	$0.243^{+0.033}_{-0.035}$	$0.629^{+0.212}_{-0.197}$
$q_{f,V}$	$\mathbf{0.115^{+0.032}_{-0.041}}$	$0.250^{+0.058}_{-0.044}$	$0.699^{+0.271}_{-0.216}$
$t_{0,pl}$	$\mathbf{7814.01^{+0.25}_{-0.22}}$	$7806.56^{+0.34}_{-0.28}$	$7810.46^{+0.03}_{-0.02}$
$u_{0,pl}$	$\mathbf{0.177^{+0.014}_{-0.013}}$	$-0.308^{+0.030}_{-0.031}$	$0.005^{+0.002}_{-0.002}$
$t_{E,pl}$ (days)	$\mathbf{-1.19^{+0.08}_{-0.09}}$	$-1.70^{+0.14}_{-0.12}$	$0.25^{+0.02}_{-0.03}$
$I_{S,total}$	$\mathbf{17.374^{+0.082}_{-0.063}}$	$17.306^{+0.081}_{-0.034}$	$17.325^{+0.080}_{-0.047}$
$q_{f,V}/q_{f,I}$	$\mathbf{1.07^{+0.18}_{-0.19}}$	$1.04^{+0.16}_{-0.14}$	$1.13^{+0.15}_{-0.12}$
s	$\mathbf{0.3382^{+0.0103}_{-0.0071}}$	$0.3144^{+0.0046}_{-0.0046}$	$3.2972^{+0.1029}_{-0.1325}$
q (10^{-4})	$\mathbf{13.60^{+1.90}_{-1.57}}$	$31.46^{+5.15}_{-5.59}$	$0.71^{+0.12}_{-0.16}$
α (deg)	$\mathbf{32.9^{+0.6}_{-0.6}}$	$20.5^{+0.8}_{-0.7}$	$205.5^{+0.9}_{-0.9}$

Note. Bold column indicates the preferred model.

an anomaly from a 1L1S model, while we analyzed an anomaly in a 2L1S model, which significantly added difficulties in analysis and computation.

In principle, we can further fit the light curve by combining any two of the four effects, e.g., the 3L1S parallax model and the 2L2S xallarap model. For example, Ryu et al. (2020) tried the 3L1S parallax model, the 2L2S parallax model, and a three-effect model (the 2L2S parallax xallarap model) for the planetary event OGLE-2018-BLG-0532. We stopped at the one-effect models because the analysis that has been done in this paper was already one of the most complicated analyses of all published microlensing events, and there are no clear prospects for further investigations. That is, it is unlikely that further investigations can break the Close/Wide degeneracy or change the nature of the planet, i.e., a Jovian-mass planet at $\sim$1 au or a super-Earth-mass to Neptune-mass planet at $\sim$6 au

(Table 7). All of the four effects can fit the long-term residuals well, and thus more dimensions would probably only loosen the constraints on each effect and decrease the $\Delta\chi^2$ between the models. Of course, one might argue that the parallax effect exists in any model anyway because of Earth's orbital motion, but a physical parallax effect for the present case, i.e., for a short ($t_{\rm E}\sim$30 days) and low-magnification ($u_0 \sim 1.3$) event, would not produce a detectable signature and thus not significantly affect the parameters of the other three effects. This is different from the Ryu et al. (2020) case, for which $t_{\rm E}\sim$140 days and thus the parallax effect played an important role.

Nevertheless, the degeneracy leads to concerns for several studies. First, the detection of isolated stellar-mass black holes from the annual microlensing parallax may need to consider the influences from the other three effects. For example, the existence of the third lens in the event, KMT-2020-BLG-0414, significantly affected the measurements of the annual microlensing parallax, and being unaware of the third lens would have led to a misjudgment of the primary lens (Zang et al. 2021b). Because the satellite microlensing parallax (Refsdal 1966; Gould 1994b) is measured by the differences between the light curves observed from Earth and a satellite or two satellites (Zhu et al. 2017), which are overwhelming compared to the differences between the annual parallax and the other effects, maybe the only robust way to make industrial-scale detections of isolated stellar-mass black holes is the satellite microlensing parallax (Gould 2023). Second, a systematic study of the stellar binaries may need to analyze only the events with clear caustic-crossing features because they must be caused by adding a lens, instead of parallax, xallarap, or adding a source. Our long-term residuals are not rare for stellar binary-lens events, which can be inferred from the three local minima that we obtained from the 2L1S grid search in Section 7.1. Including and analyzing such noncaustic-crossing features with the other three effects would be too time-consuming (and thus painful) to form a large statistical sample. Note that such pains would not be reduced for a systematic study of planets in binary systems. Although the rate of ambiguous and unambiguous planetary events is only $\sim$2% for the current KMTNet survey, adding the four effects to the 2L1S models is at least 1 order of magnitude more complicated than adding them to the 1L1S models, and the planetary rate will be higher for the future space-based microlensing projects (Roman, Penny et al. 2019; Earth 2.0, Ge et al. 2022; CSST, Yan & Zhu 2022) because of their stable photometry and complete coverage.

Another challenge is how to identify the necessity of trying these effects. The current "standard" light-curve analysis only tries the parallax effect first and only investigates more effects if the resulting parallax is detected or suspicious (e.g., by further checking for xallarap). Our case followed this procedure exactly. However, is it possible that this "standard" procedure cannot identify the clues of the other three effects even when they are detectable? It is alert that without the four effects, the "Close Inner" model is favored by $\Delta\chi^2 \geqslant 40$ over the other static models, which is significant enough to rule out the other static models, but in fact the Wide topology is preferred when considering these effects. Therefore, being unaware of these effects might lead to a wrong conclusion about the nature of the lens system (e.g., the planet).

Finally, our analysis stopped at the one-effect models, but there is currently no clear endpoint of the analysis. One can argue that each effect is possible, and thus, the microlensing modelers should explore as much as they can. Note that in the above discussion, we have not included the lens orbital motion effect. For our event, due to the low mass ratio of the secondary lens and the short-lived planetary signal, the orbital motion of the lens system has almost no effect on the light curve, but in some cases, the lens orbital motion effect can be degenerate with other effects (e.g., Batista et al. 2011; Skowron et al. 2011). In the most extreme case, there are more than 20 parameters if we consider all of the effects, which is intolerable in terms of computational resources and is likely unnecessary because the observed data cannot simultaneously provide useful constraints on all of the effects.

8. Summary

We have conducted an analysis of the microlensing planetary event, OGLE-2017-BLG-0448. The planetary signal was observed by both the KMTNet and OGLE surveys and identified by the KMTNet AnomalyFinder algorithm. To fit the planetary signal, we first tried the static 2L1S models and found two families of models: one with a low-mass-ratio wide-orbit ($s > 2$) planet (exhibiting the inner–outer degeneracy) and another (with two degenerate solutions) with a larger-mass ratio planet in a close ($s < 1$) orbit. However, there were still long-term residuals in the light curve. Thus, we further investigated the light curve by adding the microlensing parallax (the 2L1S parallax models), the microlensing xallarap (the 2L1S xallarap models), an additional lens (the 3L1S models), and an additional source (the 2L2S models). Adding these effects resulted in additional degenerate solutions and further uncertainty in the mass ratio of the planet. We also considered 1L2S with extreme xallarap models, but these turned out to be unphysical. With a Bayesian analysis, the 2L1S parallax models are excluded but the 3L1S and 2L2S models still survive. The 2L1S xallarap wide-orbit "A" model provides the best fit, with $q = 0.98 \times 10^{-4}$ and $s = 2.45^{+0.40}_{-0.30}$, and its mass ratio is lower than the previously lowest q (2.1×10^{-4}) for planets with $s > 2$ (Wang et al. 2022). However, we cannot rule out the close-orbit models with $q \sim 10^{-3}$ and $s \sim 0.35$. The wide-orbit models all contain a super-Earth-mass to Neptune-mass planet at a projected planet–host separation of $\sim$6 au and the close-orbit models all consist of a Jovian-mass planet at $\sim$1 au (Table 7).

All of the four effects can fit the light curve well and result in variations in the mass ratio between solutions that exceed the uncertainties for a given solution. Furthermore, the preference for the larger-mass ratio, close solution versus the lower-mass ratio, wide solution changes depending on which effects are included. This creates a "curse of dimensionality" in analyzing microlensing light curves and interpreting their planets. We call for more studies investigating these issues from theoretical, simulation, and statistical perspectives. These studies are urgently needed because the Roman and Earth 2.0 teams are currently building their modeling pipelines.

Acknowledgments

R.Z., W. Zang, S.M., H.Y., R.K., J.Z., and W. Zhu acknowledge support from the National Natural Science Foundation of China (grant No. 12133005). Work by R.P. and J.S. was supported

by the Polish National Agency for Academic Exchange grant "Polish Returns 2019." W. Zang acknowledges the support from the Harvard-Smithsonian Center for Astrophysics through the CfA Fellowship. This research has made use of the KMTNet system operated by the Korea Astronomy and Space Science Institute (KASI), and the data were obtained at three host sites of CTIO in Chile, SAAO in South Africa, and SSO in Australia. Data transfer from the host site to KASI was supported by the Korea Research Environment Open NETwork (KREONET). This research was supported by the Korea Astronomy and Space Science Institute under the R&D program (Project No. 2023-1-832-03) supervised by the Ministry of Science and ICT. This research uses data obtained through the Telescope Access Program (TAP), which has been funded by the TAP member institutes. Work by J.C.Y. and I.-G.S. acknowledge support from N.S.F grant No. AST-2108414. Work by C.H. was supported by the grants of the National Research Foundation of Korea (2019R1A2C2085965 and 2020R1A4A2002885). Y.S. acknowledges support from BSF grant No. 2020740. The authors acknowledge the Tsinghua Astrophysics High-Performance Computing platform at Tsinghua University for providing computational and data storage resources that have contributed to the research results reported within this paper.

Software: EMCEE (Foreman-Mackey et al. 2013), Mulens-Model (Poleski & Yee 2019), cmplx_roots_sg (Skowron & Gould 2012), VBBL (Bozza 2010; Bozza et al. 2018), triplelens (Kuang et al. 2021).

ORCID iDs

Ruocheng Zhai https://orcid.org/0009-0004-1650-3494
Radosław Poleski https://orcid.org/0000-0002-9245-6368
Weicheng Zang https://orcid.org/0000-0001-6000-3463
Andrzej Udalski https://orcid.org/0000-0001-5207-5619
Renkun Kuang https://orcid.org/0000-0003-2337-0533
Michael D. Albrow https://orcid.org/0000-0003-3316-4012
Hongjing Yang https://orcid.org/0000-0003-0626-8465
Jan Skowron https://orcid.org/0000-0002-2335-1730
Michał K. Szymański https://orcid.org/0000-0002-0548-8995
Igor Soszyński https://orcid.org/0000-0002-7777-0842
Krzysztof Ulaczyk https://orcid.org/0000-0001-6364-408X
Paweł Pietrukowicz https://orcid.org/0000-0002-2339-5899
Szymon Kozłowski https://orcid.org/0000-0003-4084-880X
Przemek Mróz https://orcid.org/0000-0001-7016-1692
Krzysztof A. Rybicki https://orcid.org/0000-0002-9326-9329
Patryk Iwanek https://orcid.org/0000-0002-6212-7221
Marcin Wrona https://orcid.org/0000-0002-3051-274X
Mariusz Gromadzki https://orcid.org/0000-0002-1650-1518
Wei Zhu https://orcid.org/0000-0003-4027-4711

References

Adams, A. D., Boyajian, T. S., & von Braun, K. 2018, MNRAS, 473, 3608
Alard, C., & Lupton, R. H. 1998, ApJ, 503, 325
Albrow, M. D. 2017, Michaeldalbrow/Pydia: Initial Release On Github., v1.0.0, Zenodo, doi:10.5281/zenodo.268049
Albrow, M. D., Horne, K., Bramich, D. M., et al. 2009, MNRAS, 397, 2099
An, J. H., Albrow, M. D., Beaulieu, J.-P., et al. 2002, ApJ, 572, 521
Batista, V., Gould, A., Dieters, S., et al. 2011, A&A, 529, A102
Batygin, K., & Brown, M. E. 2016, AJ, 151, 22
Batygin, K., Brown, M. E., & Betts, H. 2012, ApJL, 744, L3
Beaulieu, J.-P., Bennett, D. P., Fouqué, P., et al. 2006, Natur, 439, 437
Bensby, T., Yee, J. C., Feltzing, S., et al. 2013, A&A, 549, A147
Bozza, V. 2010, MNRAS, 408, 2188
Bozza, V., Bachelet, E., Bartolić, F., et al. 2018, MNRAS, 479, 5157
Dong, S., Gould, A., Udalski, A., et al. 2009, ApJ, 695, 970
Foreman-Mackey, D., Hogg, D. W., Lang, D., & Goodman, J. 2013, PASP, 125, 306
Gaia Collaboration, Brown, A. G. A., Vallenari, A., et al. 2018, A&A, 616, A1
Gaia Collaboration, Prusti, T., de Bruijne, J. H. J., et al. 2016, A&A, 595, A1
Gaudi, B. S. 1998, ApJ, 506, 533
Gaudi, B. S. 2012, ARA&A, 50, 411
Gaudi, B. S., & Gould, A. 1997, ApJ, 486, 85
Ge, J., Zhang, H., Zang, W., et al. 2022, arXiv:2206.06693
Gould, A. 1992, ApJ, 392, 442
Gould, A. 1994a, ApJL, 421, L71
Gould, A. 1994b, ApJL, 421, L75
Gould, A. 2000, ApJ, 542, 785
Gould, A. 2023, arXiv:2310.19164
Gould, A., & Loeb, A. 1992, ApJ, 396, 104
Gould, A., Udalski, A., Monard, B., et al. 2009, ApJL, 698, L147
Griest, K., & Hu, W. 1992, ApJ, 397, 362
Han, C. 2005, ApJ, 629, 1102
Han, C. 2006, ApJ, 638, 1080
Han, C., Chang, H.-Y., An, J. H., & Chang, K. 2001, MNRAS, 328, 986
Holman, M. J., & Wiegert, P. A. 1999, AJ, 117, 621
Holtzman, J. A., Watson, A. M., Baum, W. A., et al. 1998, AJ, 115, 1946
Hwang, K.-H., Choi, J.-Y., Bond, I. A., et al. 2013, ApJ, 778, 55
Jiang, G., DePoy, D. L., Gal-Yam, A., et al. 2004, ApJ, 617, 1307
Jung, Y. K., Gould, A., Udalski, A., et al. 2019b, AJ, 158, 28
Jung, Y. K., Gould, A., Zang, W., et al. 2019a, AJ, 157, 72
Kennedy, G. M., & Kenyon, S. J. 2008, ApJ, 673, 502
Kim, D.-J., Kim, H.-W., Hwang, K.-H., et al. 2018, AJ, 155, 76
Kim, S.-L., Lee, C.-U., Park, B.-G., et al. 2016, JKAS, 49, 37
Kuang, R., Mao, S., Wang, T., Zang, W., & Long, R. J. 2021, MNRAS, 503, 6143
Kuang, R., Zang, W., Jung, Y. K., et al. 2022, MNRAS, 516, 1704
Mao, S., & Paczynski, B. 1991, ApJL, 374, L37
Miyazaki, S., Sumi, T., Bennett, D. P., et al. 2020, AJ, 159, 76
Morbidelli, A., Bitsch, B., Crida, A., et al. 2016, Icar, 267, 368
Nataf, D. M., Gould, A., Fouqué, P., et al. 2013, ApJ, 769, 88
Nesvorný, D., & Morbidelli, A. 2012, AJ, 144, 117
Paczyński, B. 1986, ApJ, 304, 1
Penny, M. T., Gaudi, B. S., Kerins, E., et al. 2019, ApJS, 241, 3
Poindexter, S., Afonso, C., Bennett, D. P., et al. 2005, ApJ, 633, 914
Poleski, R., Skowron, J., Udalski, A., et al. 2014, ApJ, 795, 42
Poleski, R., & Yee, J. C. 2019, A&C, 26, 35
Refsdal, S. 1966, MNRAS, 134, 315
Rota, P., Hirao, Y., Bozza, V., et al. 2021, AJ, 162, 59
Ryu, Y.-H., Hwang, K.-H., Gould, A., et al. 2019, AJ, 158, 151
Ryu, Y.-H., Udalski, A., Yee, J. C., et al. 2020, AJ, 160, 183
Skowron, J., & Gould, A. 2012, arXiv:1203.1034
Skowron, J., Udalski, A., Gould, A., et al. 2011, ApJ, 738, 87
Skowron, J., Udalski, A., Kozłowski, S., et al. 2016, AcA, 66, 1
Suzuki, D., Bennett, D. P., Sumi, T., et al. 2016, ApJ, 833, 145
Szymański, M. K., Udalski, A., Soszyński, I., et al. 2011, AcA, 61, 83
Thommes, E. W., Duncan, M. J., & Levison, H. F. 1999, Natur, 402, 635
Tomaney, A. B., & Crotts, A. P. S. 1996, AJ, 112, 2872
Tsiganis, K., Gomes, R., Morbidelli, A., & Levison, H. F. 2005, Natur, 435, 459
Udalski, A. 2003, AcA, 53, 291
Udalski, A., Ryu, Y.-H., Sajadian, S., et al. 2018, AcA, 68, 1
Udalski, A., Szymański, M. K., & Szymański, G. 2015, AcA, 65, 1
Wang, H., Zang, W., Zhu, W., et al. 2022, MNRAS, 510, 1778
Wozniak, P. R. 2000, AcA, 50, 421
Yan, S., & Zhu, W. 2022, RAA, 22, 025006
Yang, H., Mao, S., Zang, W., & Zhang, X. 2021, MNRAS, 502, 5631
Yang, H., Yee, J. C., Hwang, K.-H., et al. 2024, MNRAS, 528, 11
Yee, J. C., Shvartzvald, Y., Gal-Yam, A., et al. 2012, ApJ, 755, 102
Zang, W., Han, C., Kondo, I., et al. 2021b, RAA, 21, 239
Zang, W., Hwang, K.-H., Udalski, A., et al. 2021a, AJ, 162, 163
Zang, W., Jung, Y. K., Yang, H., et al. 2023, AJ, 165, 103
Zang, W., Yang, H., Han, C., et al. 2022, MNRAS, 515, 928
Zhang, J., Zang, W., Jung, Y. K., et al. 2023, MNRAS, 522, 6055
Zhu, W., Udalski, A., Huang, C. X., et al. 2017, ApJL, 849, L31